

1 **Revealing Hidden Oxygen Variability in the North Pacific: A Two-**  
2 **Decade Analysis Using GOBAI-O<sub>2</sub>**

3  
4

5 Miho Ishizu<sup>1,2</sup>, Tomomichi Ogata<sup>3</sup>

6

7 *<sup>1</sup>Center for Climate Physics, Institute for Basic Science, Busan 46241, Republic of Korea*

8 *<sup>2</sup>Pusan National University, Tonghapgigyegwan Bldg 2 Busandaehak-ro, 63 beon-gil, Geumjeong-gu,*  
9 *Busan 46241, Republic of Korea*

10 *<sup>3</sup>Japan Agency for Marine-Earth Science and Technology, Environmental Variability Prediction and*  
11 *Application Research Group, Yokohama Institute for Earth Sciences, 3173-25 Showa-machi,*  
12 *Kanagawa-ku, Yokohama 236-0001, Japan*

13 To whom correspondence may be addressed. Email: [mishizu@pusan.ac.kr](mailto:mishizu@pusan.ac.kr)

14

15

16 **Abstract**

17 Oceanic dissolved oxygen concentrations are thought to be declining under ongoing global warming,  
18 yet their variability remains less well understood than that of physical parameters such as temperature  
19 and salinity, primarily due to the limited spatial and temporal coverage of oxygen observation. Here,  
20 we examine linear trends in potential temperature, salinity, and dissolved oxygen in the North Pacific  
21 over the past two decades ( 2004–2023 ), using the GOBAI-O<sub>2</sub> dataset. We compare the diagnosed  
22 oxygen trends with those of physical parameters to reveal the spatial structure of recent changes. The  
23 oxygen trends inferred from GOBAI-O<sub>2</sub> are broadly consistent with trends observed along ship-based  
24 hydrographic repeat lines. While basin-scale deoxygenation is evident, we also identify localized  
25 oxygen increases on specific density surfaces. By relating these patterns to the surrounding physical

26 environment, we find that the spatial heterogeneity in oxygen trends is consistent with known  
27 oceanographic processes, including the southward retreat of the oxygen minimum layer and the  
28 northward migration of a front separating the subtropical and subarctic gyres. These results underscore  
29 the value of GOBAI-O<sub>2</sub> data in linking physical variability to previously unrecognized biological and  
30 biogeochemical patterns in the ocean.

31

32

### 33 **Plain Language Summary**

34 1. We investigated how potential temperature, salinity, and dissolved oxygen have changed in the  
35 North Pacific over the past 20 years using GOBAI-O<sub>2</sub> dataset, and we examined the physical  
36 processes responsible for these trends.

37 2. The trends identified in this study are broadly consistent with findings from previous research, and  
38 improved spatial coverage of GOBAI-O<sub>2</sub> allowed us to reveal connections between regional  
39 patterns that we previously only partially understood.

40 3. Overall, dissolved oxygen decreased across much of the North Pacific. However, some regions  
41 showed increasing oxygen levels, indicating that the changes were not uniform. These non-uniform  
42 patterns reflect known physical ocean processes. For example, higher oxygen levels in the northern  
43 North Pacific are consistent with a northward shift of the front separating the subtropical and  
44 subarctic gyres. In the equatorial Pacific, the reduced westward extent of the oxygen minimum  
45 layer corresponds to a weakening and poleward shift of the North Equatorial Countercurrent  
46 ( NECC ) on interdecadal timescales.

47 4. These findings provide new evidence that links large-scale physical ocean changes to previously  
48 unclear changes in biological and biogeochemical observations.

49

50 Keywords: dissolved oxygen, 20-year linear trends, Bio-Argo float data, global warming

51

## 52 **1. Introduction**

53 Over recent decades, the global ocean has experienced a decline in its dissolved oxygen inventory, a  
54 trend projected to continue through the 21st century [ Keeling et al., 2010; Breitburg et al., 2018;  
55 Stramma and Schmidtko, 2021; Limburg et al., 2020; Ito et al., 2017, 2024; Kolodziejczyk et al., 2024 ].  
56 This deoxygenation is driven in part by reduced ocean oxygen solubility under rising sea-surface  
57 temperatures, which promotes oxygen outgassing. In addition, enhanced stratification and a slowdown  
58 of ocean circulation under global warming can reduce interior ventilation and oxygen supply [ Keeling  
59 et al., 2010; Bopp et al. 2013; Ito et al. 2017 ]. Ocean oxygen loss can negatively affect aerobic marine  
60 organisms [ Pörtner and Farrell, 2008; Sampaio et al., 2021 ], alter biogeochemical cycles, and  
61 potentially induce climate-relevant feedback [ Berman-Frank et al., 2008 ]. Historical deoxygenation  
62 has been inferred from globally distributed observations [ Helm et al., 2011; Schmidtko et al., 2017;  
63 Ito et al., 2017; Takatani et al., 2012; Sasano et al., 2015; Lauvset et al., 2022b ], and Earth system  
64 models have been used to simulate both historical and future changes in ocean oxygen [ Bopp et al.,  
65 2013; Kwiatkowski et al., 2020; Li et al. 2020 ].

66

67 Observed oxygen trends have traditionally been assessed using the discrete measurements of dissolved  
68 oxygen concentration (  $O_2$  ), typically obtained by Winkler titration [ Winkler, 1988 ]. These  
69 measurements are also used to calibrate electrode- and, more recently, optode-based oxygen sensors  
70 mounted on conductivity-temperature-depth ( CTD ) profilers [ Helm et al. 2011; Schmidtko et al.,  
71 2017; Lauvset et al., 2022b ]. Although programs such as WOCE, CLIVAR, and GO-SHIP have  
72 collected high-quality oxygen measurements globally, repeat occupation intervals are commonly on  
73 the order of a decade, limiting the ability to robustly quantify annual to seasonal variability. Higher-

74 frequency ship-based observations exist in a few regions [ Takatani et al. 2012; Sasano et al., 2015 ],  
75 but their spatial coverage is limited. Consequently, despite attempts to characterize basin-scale patterns  
76 [ Ito et al. 2017; Stramma et al. 2020; Kolodziejczyk et al. 2024 ], observational constraints have  
77 hampered a spatially and temporally comprehensive understanding of dissolved oxygen variability and  
78 trends.

79

80 Oxygen sensors were first deployed on Argo profiling floats in the mid-2000s. Since then,  
81 approximately 1,800 oxygen-equipped floats have been deployed worldwide, substantially advancing  
82 the observational basis for assessing oxygen variability and trends [ Sharp et al., 2023 ]. The expansion  
83 toward a global biogeochemical ( BGC ) Argo network has improved sampling in regions that were  
84 previously sparsely observed [ Claustre et al., 2020 ]. In parallel, major progress has been made in  
85 calibration, adjustments, and quality control of oxygen measurements, including pre-deployment drift  
86 corrections [ D'Asaro and McNeil, 2013; Johnson et al., 2015; Bittig and Körtzinger, 2015; Bushinsky  
87 et al., 2016; Drucker and Riser, 2016; Nicholson and Feen, 2017 ], climatology-based calibrations  
88 [ Takeshita et al., 2013 ], in-air oxygen measurement calibrations [ Körtzinger et al., 2005; Bittig and  
89 Körtzinger, 2015; Johnson et al., 2015; Bushinsky et al., 2016 ], post-deployment drift corrections  
90 [ Johnson et al., 2017; Bittig et al., 2018a, b ], and the standardized delayed-mode quality control  
91 procedures [ Maurer et al., 2021 ]. Together, these developments have reduced uncertainty and  
92 improved the consistency of optode-based [ O<sub>2</sub> ] measurements from Argo floats.

93

94 To date, oxygen observations from Argo floats have been used primarily in regional process studies,  
95 including air-sea oxygen exchange [ Wolf et al., 2018 ], upper-ocean primary production [ Alkire et al.,  
96 2012; Estapa et al., 2019 ], biological pump efficiency [ Johnson and Bif, 2021 ], and the dynamics of  
97 the oxygen minimum zone [ Udaya Bhaskar et al., 2021 ]. Recently, Sharp et al. [ 2023 ] produced a

98 four-dimensional gridded [ O<sub>2</sub> ] product, GOBAI-O<sub>2</sub> ( Gridded Ocean Biogeochemistry from Artificial  
99 Intelligence ( AI ) – Oxygen ). GOBAI-O<sub>2</sub> is constructed using machine-learning methods trained on  
100 oxygen observations and designed to reconstruct spatial patterns, seasonal cycles, and decadal  
101 variability, particularly in regions where observational data gaps coincide with high background O<sub>2</sub>  
102 variability.

103

104 In the North Pacific, several studies have documented heterogeneous oxygen trends. Using an  
105 objectively mapped monthly climatology of O<sub>2</sub> based on the World Ocean Database 2013 ( WOD13 )  
106 [ Boyer et al. 2013 ], Ito et al. [ 2017 ] reported multidecadal variability and trends in dissolved O<sub>2</sub> in  
107 the surface-layer oxygen from 1958 to 2013. Sasano et al. [ 2015 ], using the high-frequency shipboard  
108 sections along the 137°E and 165°E lines from 1987 to 2011, reported oxygen declines in the northern  
109 subtropical to subtropical-subarctic transition zones of  $-0.45 \pm 0.16 \mu\text{mol/kg/yr}$  at 25.3  $\sigma_{\theta}$  and  $-0.45 \pm$   
110  $0.14 \mu\text{mol/kg/yr}$  at 26.8  $\sigma_{\theta}$ , respectively. They also identified a significant oxygen increase in the  
111 tropical Oxygen Minimum Layer (OML) of  $+0.36 \pm 0.004 \mu\text{mol/kg/yr}$ , highlighting pronounced spatial  
112 heterogeneity in oxygen trends. At broader scales, Stramma et al. [ 2020 ] analyzed historical bottle  
113 data and reported links between oxygen variability and climate modes such as the Pacific Decadal  
114 Oscillation ( PDO ) and the North Pacific Gyre Oscillation (NPGO), although sparse sampling makes  
115 it difficult to robustly connect regional trends to physical mechanisms. Collectively, previous studies  
116 indicate that oxygen changes in the North Pacific can be strong, spatially non-uniform, and potentially  
117 driven by both circulation/ventilation changes and biologically mediated oxygen consumption  
118 [ Sasano et al. 2015; 2018; Ito et al. 2017; 2024; Stramma et al., 2020; Kolodziejczyk et al. 2024 ].

119

120

121 Because observational opportunities to quantify trends in dissolved oxygen—together with concomitant  
122 changes in temperature and salinity—remain limited, gridded products such as GOBAI-O<sub>2</sub> are

123 becoming increasingly valuable for basin-scale analyses. In this study, we use GOBAI-O<sub>2</sub> to quantify  
124 linear trends in potential temperature, salinity, and dissolved oxygen in the North Pacific over 2004–  
125 2023 and examine how their trends are connected in both depth and density space. We further discuss  
126 the extent to which the diagnosed oxygen trends can be interpreted in terms of physical drivers,  
127 including surface warming, stratification changes, and circulation variability in the North Pacific.

128

## 129 **2. Data and Methods**

### 130 **2.1 GOBAI-O<sub>2</sub> dataset**

131 We use GOBAI-O<sub>2</sub>, a four-dimensional, monthly gridded product of dissolved oxygen ( O<sub>2</sub> ) in the  
132 ocean interior, generated using machine learning ( ML ) algorithms trained on both Argo float oxygen  
133 measurements and ship-based discrete observations [ Sharp et al., 2023 ]. GOBAI-O<sub>2</sub> is mapped onto  
134 the temperature-salinity fields provided by the global Argo array [ Roemmich and Gilson, 2009 ]. The  
135 underlying oxygen training database combines ship-based measurements from GLODAPv2.2022 and  
136 Argo float data distributed through the Argo Global Data Assembly Centers, after quality control  
137 [ Sharp et al., 2023 ] ( <https://doi.org/10.25921/z72m-yz67> ).

138

139 According to Sharp et al. [ 2023 ], the float data used in GOBAI-O<sub>2</sub> were filtered to retain only delayed-  
140 mode adjusted profiles with quality flags of 1 (good), 2 (probably good), or 8  
141 (interpolated/extrapolated) for pressure, temperature, salinity, and dissolved oxygen. Among all  
142 available float profiles, 51.4% underwent quality control through comparison with climatological  
143 fields from the World Ocean Atlas (WOA) or the Commonwealth Scientific and Industrial Research  
144 Organisation Regional Sea Atlas (CARS). An additional 30.3% were evaluated using atmospheric  
145 oxygen concentration measurements, and 7.0% were quality controlled through comparison with in-  
146 water measurements (WOD, OMS assuming an oxygen zero, or deployment-time CTD profiles). A

147 further 5.3% were adjusted using in-situ optode calibration based on the method of Drucker and Riser  
148 [2016], 3.3% were adjusted by other methods, 1.9% were unclassified, and the remaining 0.9% were  
149 not adjusted.

150  
151 The ML models predict O<sub>2</sub> using predictors that include absolute salinity, conservative temperature,  
152 potential density anomaly, hydrostatic pressure, bottom depth, and additional spatiotemporal  
153 covariates representing geographic, seasonal, and interannual variability. Biological processes are not  
154 explicitly parameterized in the ML framework; however spatiotemporal covariates can implicitly  
155 capture biological influences to some extent [ Giglio et al., 2018 ].

156  
157 GOBAI-O<sub>2</sub> is produced using two ML approaches: feed-forward networks (FNNs) and random forest  
158 regression ( RFRs, [ Breiman, 2001 ] ). The final O<sub>2</sub> estimate at each grid point is taken as the mean  
159 of the FNN and RFR predictions. The dataset spans 2004–2023 at monthly resolution on a 1° × 1°  
160 latitude –longitude grid, covering 86% of the global ocean area. The product is provided on 58 vertical  
161 levels from the surface to ~2,000 m. Sharp et al. [ 2023 ] reported 0.79 ± 0.04% per decade decrease  
162 in the oxygen inventory of the upper 2000 m over 2004–2022. Full details of their data sources,  
163 processing, algorithm training, evaluation, and uncertainty estimation are given in Sharp et al. [ 2023 ].

## 165 2.2 Uncertainty estimates

166 GOBAI-O<sub>2</sub> provides an uncertainty estimate for each gridded O<sub>2</sub> value, constructed by combining  
167 independent uncertainty components in quadrature [ Sharp et al., 2023 ]:

$$168 \quad u([O_2])_{tot.} = \sqrt{u([O_2])_{meas.}^2 + u([O_2])_{grid.}^2 + u([O_2])_{alg.}^2} \quad (1),$$

169 where  $u([O_2])_{meas.}^2$  represents measurement uncertainty of the underlying observations,

170  $u([O_2])_{grid}^2$  ) is the gridding uncertainty associated with representing a four-dimensional  
171 spatiotemporal volume by a single value, and  $u([O_2])_{alg}^2$  is the algorithmic uncertainty arising from  
172 the ML estimation. We use  $u([O_2])_{tot}$  to characterize uncertainty in  $O_2$  and to propagate uncertainty  
173 into our oxygen trend estimates (Figs. 1–4). In most figures, we incorporate the mean uncertainty when  
174 estimating linear  $O_2$  trends.

175

### 176 **2.3 Vertical grid and interpolation for isopycnal analysis**

177 GOBAI- $O_2$  is provided on a  $1^\circ \times 1^\circ$  horizontal grid with 58 depth levels: 2.5, 10, 30, 40, 50, 60, 70,  
178 80, 90, 100, 110, 120, 130, 140, 150, 160, 170, 182.5, 200, 220, 240, 260, 280, 300, 320, 340, 360,  
179 380, 400, 420, 440, 462.5, 500, 550, 600, 650, 700, 750, 800, 850, 900, 950, 1000, 1050, 1100, 1150,  
180 1200, 1250, 1300, 1350, 1412.5, 1500, 1600, 1700, 1800, 1900 and 1975 m. The enhanced near-surface  
181 vertical resolution is important for resolving strong gradients in temperature, salinity, density, and  
182 oxygen within the mixed layer [ Kara et al., 2000 ].

183

184 For analysis performed in density space, we interpolate the original depth-level data to 1-m vertical  
185 grid using cubic spline interpolation and then evaluate linear trends on a  $1^\circ \times 1^\circ \times 1$  m grid. This  
186 approach enables computation of trends as a function of latitude (  $1^\circ$  bins ) and potential density  
187 anomaly (  $0.1\sigma_\theta$  bins ) ( Figs. 4–7 ). To evaluate sensitivity to interpolation choices, we repeated the  
188 analysis using linear, shape-preserving cubic ( PCHIP ) interpolation and using coarser vertical grids  
189 ( 2 m and 5 m ). The resulting trend patterns show no material differences among interpolation methods  
190 ( Figs. S1 ( a, b ) and S2 ( a, b ) ). The 5-m grid cannot resolve densities lighter than  $24.0\sigma_\theta$  at some  
191 latitudes; however, the main features are preserved across all tested resolutions.

192

### 193 **2.4 OFES model output**

194 In Section 3.3.2, we additionally use output from the eddy-resolving OGCM for the Earth Simulator  
195 ( OFES ) [ Masumoto et al., 2004; 2010; Sasaki et al., 2008 ] to examine the physical context of the  
196 diagnosed variability. OFES is based on the MOM3 [ Pacanowski and Griffies, 2000 ] and uses a quasi-  
197 global domain spanning 75° S– 75°N with 0.1° x 0.1° horizontal resolution and 54 vertical levels. The  
198 model was initialized from rest using the World Ocean Atlas 1998 (WOA98) [ Boyer and Levitus,  
199 1997 ], and spun up for 50 years using climatological forcing derived from NCEP-NCAR reanalysis  
200 [ Kalnay et al., 1996 ]. After spin-up, a hindcast experiment was conducted from 1950 to 2024 using  
201 daily NCEP-NCAR forcing. Here we analyze OFES output over 1950–2023.

202

## 203 **2.5 GODAS model output**

204 In Section 3.3.2, we also use temperature and salinity fields from the NCEP Global Ocean Data  
205 Assimilation System ( GODAS ) to complement our analysis. GODAS is a global ocean reanalysis  
206 system developed at the National Centers for Environmental Prediction ( NCEP ) and is based on the  
207 Modular Ocean Model version 3 [ Pacanowski and Griffes, 2000 ]. The system assimilates surface  
208 temperature profiles, XBT data, moored buoy observations, and other in situ measurements using a  
209 three-dimensional variational ( 3DVAR ) assimilation scheme [ Behringer and Xue, 2004; Behringer,  
210 2007 ]. The GODAS reanalysis is provided on a 1° x 1° horizontal grid with enhanced meridional  
211 resolution (1/3°) near the equator and includes 40 vertical levels. The reanalysis spans from 1980 to  
212 the present and is widely used for climate diagnostics and ocean variability studies. In this study, we  
213 analyze GODAS density fields over the period 2003-2024 by using temperature and salinity.

214

## 215 **3. Results**

### 216 **3.1 Horizontal distributions of linear trends**

217 Figure 1 illustrates the horizontal and vertical distributions of linear trends in potential temperature,

218 salinity, and dissolved oxygen (  $O_2$  ), over 2004–2023. Positive trends in potential temperature are  
219 primarily confined to the surface layer above 200 m depth ( Fig. 1a–c ), with larger magnitudes at  
220 higher latitudes. In contrast, negative trends emerge below the surface in the eastern tropical area  
221 (  $180^\circ$ – $120^\circ$ W,  $5^\circ$ – $15^\circ$ N ) ( Fig. 1b ), extending westward and deepening with increasing depth ( Fig.  
222 1d–f ). Below  $\sim$ 400 m, the spatial distributions of positive and negative temperature trends differ  
223 between the subarctic and subtropical gyres.

224

225 Salinity trends exhibit generally negative values throughout the surface layer ( Fig. 1h–i ), consistent  
226 with freshening. Localized positive salinity trends are detected in the Kuroshio–Oyashio transition  
227 area and the northwest Pacific (  $140^\circ$ – $180^\circ$ E,  $20^\circ$ – $50^\circ$ N ), as well as in the tropical region (  $120^\circ$ –  
228  $170^\circ$ E,  $0^\circ$ – $10^\circ$ N ). Additional positive trends appear along the eastern boundary off California (  $130^\circ$ –  
229  $199^\circ$ W,  $20^\circ$ – $40^\circ$ N ). Below 200 m depth, salinity trends are weaker and broadly mirror the temperature  
230 ones ( Fig. 1j–k ). Notably, negative salinity trends are evident around the Alaska gyre (  $170^\circ$ – $130^\circ$ W,  
231  $40^\circ$ – $55^\circ$ N ) ( Fig. 1j–l ), a pattern that differs from the corresponding temperature trends.

232

233 Negative trends in dissolved  $O_2$  are widespread across the North Pacific and extend throughout much  
234 of the water column ( Fig. 1o–u ). Large negative trends are concentrated at higher latitudes near the  
235 surface, with their locations shifting systematically with depth. Particularly strong  $O_2$  declines are  
236 observed along the northeastern boundary (  $140^\circ$ – $130^\circ$ W,  $40^\circ$ – $50^\circ$ N ) and within the southern  
237 subtropical region (  $10^\circ$ – $25^\circ$ N ) on density surfaces between 25.2 and  $26.8\sigma_\theta$ , corresponding to depths  
238 of approximately 200–600 m ( Fig. 1q–s ). In contrast, weak positive  $O_2$  trends are detected below 200  
239 m depth in the Kuroshio–Oyashio transition zone (  $130^\circ$ – $150^\circ$ E,  $30^\circ$ – $40^\circ$ N ), extending into deeper  
240 layers and spreading northeastward across the basin ( Fig. 1r–u ).

241

242 Positive O<sub>2</sub> trends are restricted to specific regions and depths: the tropical region at ~100 m depth  
243 ( Fig. 1p ); the Alaska Gyre at 200–400 m depth ( Fig. 1q–r ); the western tropical region at 400–600  
244 m depth ( Fig. 1r–s ); and the Kuroshio–Oyashio transition region at similar depths ( Fig. 1r–s ). When  
245 examined as a function of latitude, the magnitudes of negative O<sub>2</sub> trends do not depend monotonically  
246 on latitude alone. While surface-layer declines are strongest at high latitudes, the largest negative  
247 trends at intermediate depths ( 400–600 m ) occur in the mid-latitude band ( 30°–40°N ). This depth-  
248 dependent latitudinal structure implies the importance of remote transports and the circulation-driven  
249 redistribution of oxygen, rather than purely local surface forcing. The underlying mechanisms are  
250 discussed further in Section 3.3.

251

252 The total uncertainty in dissolved O<sub>2</sub>,  $u([O_2])_{tot.}$ , exhibits pronounced regional structure ( Fig. 2a–  
253 g ). Uncertainty is largest in the North Pacific north of 50°N and decreases toward lower latitudes.  
254 Relatively high uncertainty values are also evident in the surface layer, and within regions of strong  
255 density gradients in the eastern tropical Pacific [150°–120°W, 10°–30°N] at depths of 100–200 m ( Fig.  
256 2b–c ). In general, uncertainty peaks near 100 m depth and decreases with increasing depth ( Fig. 2  
257 and Figure A14 in Sharp et al. [ 2023 ] ). As shown by Sharp et al. [ 2023 ], regionally variations in  
258 uncertainty are dominated by algorithmic uncertainty rather than measurement or gridding components  
259 ( Eq. 1 ). Elevated algorithmic uncertainty in the northern Pacific above 50°N and along the western  
260 and eastern tropical margins below 20°N reflects sparse observational coverage in these regions  
261 ( Figure 1 in Sharp et al. 2023 ).

262

263 To assess whether regional trends exceed the dataset uncertainty, we computed the spatial distribution  
264 of Robustness (  $R$  ), defined as  $R = |\text{trend over two decades}| / \text{uncertainty}$  ( Fig. 1v–bb ). This  
265 diagnostic identifies regions in which the magnitude of the trend is sufficiently large to be considered

266 physically robust. The results indicate that R exceeds or approaches high values in the eastern and  
267 western tropical zones, the Kuroshio Extension region, portions of the subpolar North Pacific, and  
268 along the 27.2–27.4  $\sigma_\theta$  density surfaces at 800–1000 m depth. Based on this metric, larger oxygen  
269 trend magnitudes correspond to higher R values, indicating greater robustness. Thus, in the upper  
270 ocean ( 2.5–100 m ), trends are physically robust mainly in the northern North Pacific. At 200–400 m,  
271 robust signals appear both in the northern North Pacific and along the 25.2–26.0  $\sigma_\theta$  surfaces in the  
272 southern subtropical region, as well as in the eastern and western tropics. At 600–1000 m, the trends  
273 are robust within the subtropical gyre bounded by the 27.0  $\sigma_\theta$  surface.

274

275 Compared with the historical horizontal distributions of dissolved O<sub>2</sub> reported by Ito et al. [ 2017 ]  
276 ( Figure 3 in Ito et al. 2017 ), our analysis reveals a broader spatial extent of negative trends across the  
277 North Pacific. Whereas data gaps increase with depth in Ito et al. [ 2017 ], the GOBAI-O<sub>2</sub> product  
278 provides more spatially continuous coverage, yielding distributions that remain consistent with  
279 surrounding regions. In addition, positive O<sub>2</sub> trends detected here in the Kuroshio–Oyashio transition  
280 zone and the northeastern North Pacific on density surfaces of 26.8–27.0 $\sigma_\theta$  ( Fig. 1r ) were not clearly  
281 evident in the earlier climatology-based analysis. Similarly, the positive trends identified in the western  
282 tropical Pacific below 400 m depth ( Fig. 1r–t ) are stronger and more spatially coherent than those  
283 reported previously.

284

285 The positive O<sub>2</sub> trends coincide with regions of relatively low uncertainty values ( Fig. 1p–s and 1w–  
286 y ), suggesting that they are robust features supported by the high observation density of Argo profiling  
287 floats. Other regions exhibiting positive signals—the northeastern North Pacific with a density range  
288 of 26.8–27.0 $\sigma_\theta$  ( 170°E–150°W, 45–55°N, Fig. 1r ) and the tropical western Pacific ( 130°–170°E, 0°–

289 10°N, Fig. 1r–t )—also correspond to areas of low uncertainty ( Fig. 1y–aa ). Consequently, these  
290 signals likely represent genuine regional reoxygenation superimposed on the basin-scale  
291 deoxygenation trend.

292

293 Some localized expansions of the trend patterns, particularly in the tropical eastern Pacific ( e.g. 170°–  
294 130°W, 0°–20°N ) may partly reflect regions of elevated uncertainty, occasionally exceeding 15  
295  $\mu\text{mol/kg}$  ( Fig. 1q–s; Fig. 4i ). Such large uncertainties arise from sparse observations and high  
296 background variability [ Sharp et al. 2023 ]. Additional bias may stem from sensor calibration  
297 limitations in Argo oxygen measurements, especially in oxycline regions where finite optode response  
298 times can introduce systematic errors [ Bittig et al., 2014; 2018a,b ]. Despite these caveats, the spatial  
299 patterns of the diagnosed  $\text{O}_2$  trends are generally smooth and coherent across the basin. Based on  
300 statistical significance testing, most trends are significant throughout the water column ( Fig. 1o–u ),  
301 allowing them to be interpreted in the context of established physical processes in the North Pacific.  
302 Overall, the GOBAI- $\text{O}_2$  dataset provides an improved framework for diagnosing basin-scale oxygen  
303 variability and its physical drivers.

304

### 305 **3.2 Vertical sections and isopycnal density analysis of linear trends in 137°E and 165°E lines**

306 To facilitate direct comparison with historical ship-based observations, we examine vertical sections  
307 and isopycnal distributions of linear trends in potential temperature, salinity, and dissolved  $\text{O}_2$  along  
308 the 137°E and 165°E meridional sections ( Fig. 3 ). Ogata and Nonaka [ 2020 ] analyzed salinity data  
309 from 20 years of shipboard observations along the 137°E line between 1997 and 2016, while Sasano  
310 et al. [ 2015 ] analyzed temperature, salinity, and dissolved  $\text{O}_2$  data from 25 years of cruises along the  
311 165°E line between 1987 and 2011.

312

313 Along both sections, large negative trends in potential temperature and salinity are concentrated along  
314 the 25.0–26.0 $\sigma_\theta$  isopycnal surfaces, corresponding to potential temperatures of approximately 10–  
315 12°C and salinities of 34.4–34.5 ( Fig. 3a, b, e, f ). In contrast, the strongest negative trends in dissolved  
316 O<sub>2</sub> occur primarily along denser isopycnals between 26.0 and 27.0 $\sigma_\theta$  ( Fig. 3c, g ). This vertical  
317 separation indicates that the regions of pronounced oxygen decline are not co-located with those of  
318 temperature and salinity trends, implying distinct controlling mechanisms.

319

320 In addition to widespread oxygen declines, pronounced positive O<sub>2</sub> trends are detected south of ~15°N  
321 below 200 m depth along the 137°E line ( Fig. 3c ). These positive trends are located near the upper  
322 boundary of the oxygen minimum layer ( OML ). Comparison with the corresponding uncertainty  
323 distributions ( Fig. 3d, h ) shows that regions exhibiting positive or negative oxygen trends generally  
324 do not coincide with areas of elevated uncertainty, indicating that these signals are robust within the  
325 GOBAI-O<sub>2</sub> framework.

326

327 The distributions of linear trends on isopycnal surfaces further highlight differences among  
328 temperatures, salinity, and dissolved O<sub>2</sub> ( Fig. 4 ). Trends in temperature and salinity are closely aligned,  
329 with warming accompanied by salinification and cooling accompanied by freshening ( Fig. 4a–b, d–  
330 e ). In the tropical region ( 5°S–5°N ), distinct positive trends in both variables are evident over the  
331 density range of 22.0–26.0 $\sigma_\theta$ . In contrast, little systematic trend is detected in the salinity minimum  
332 region ( S = 34–34.1 ) within the density range of 26.5–27.0 $\sigma_\theta$ . At higher latitudes ( 40°–50°N ), strong  
333 positive trends in both temperature and salinity are observed along the 26.0–27.0 $\sigma_\theta$  surfaces ( Fig. 4e ).

334

335 Dissolved oxygen trends exhibit a markedly different structure. Although negative O<sub>2</sub> trends dominate

336 overall, weak but coherent positive trends appear across the density range  $23.0\text{--}26.0\sigma_\theta$  in low-latitude  
337 regions (  $5^\circ\text{S}\text{--}5^\circ\text{N}$  ). More pronounced positive  $\text{O}_2$  trends are detected in the deeper density range of  
338  $26.0\text{--}27.0\sigma_\theta$  between  $5^\circ$  and  $10^\circ\text{N}$ . Additional weak positive trends are observed between  $10^\circ$  and  
339  $20^\circ\text{N}$  within the density range of  $23.0\text{--}25.0\sigma_\theta$  along both the  $137^\circ\text{E}$  and  $165^\circ\text{E}$  sections.

340

341 Compared with previous studies, the GOBAI- $\text{O}_2$ -based trends reveal both similarities and notable  
342 differences. The general characteristics of temperature and salinity trends are broadly consistent with  
343 those reported by Sasano et al. [ 2015 ], although the present results are spatially smoother, particularly  
344 for dissolved oxygen. This smoothness likely reflects the gridded nature of the dataset and the spatial  
345 regularization inherent in the machine-learning reconstruction. Along the  $137^\circ\text{E}$  section, the GOBAI-  
346  $\text{O}_2$  temperature and salinity fields exhibit a wider area of negative salinity trends within the density  
347 range  $22.0\text{--}24.0\sigma_\theta$  than those reported by Ogata and Nonaka [ 2020 ] using OFES output.

348

349 Ship-based observations by Sasano et al. [ 2015 ] identified patchy positive trends in oxygen within  
350 the density range  $24.5\text{--}27.5\sigma_\theta$  in the regions (  $5^\circ\text{--}15^\circ\text{N}$  and  $6^\circ\text{S}\text{--}1^\circ\text{N}$  ), as well as localized positive  
351 trends at greater depths. In contrast, the GOBAI- $\text{O}_2$  data reveal a broader, smoother, and more spatially  
352 coherent pattern of positive  $\text{O}_2$  trend spanning  $6^\circ\text{S}$  to  $5^\circ\text{N}$ . At the same time, the present analysis more  
353 clearly delineates the core regions of negative oxygen trends between  $5^\circ$  and  $15^\circ\text{N}$  along the lower  
354 isopycnals ( Fig. 3c and f ), which are characteristic of the subtropical gyre. These differences  
355 underscore the complementary nature of ship-based observations and gridded reconstructions and  
356 highlight the advantage of GOBAI- $\text{O}_2$  for resolving basin-scale and isopycnal-scale oxygen variability.

357

### 358 **3.3 Horizontal distribution of linear trends along isopycnal surfaces**

#### 359 **3.3.1 Potential temperature and salinity**

360 The horizontal distributions of linear trends in potential temperature, salinity, and dissolved oxygen on  
361 specific isopycnal surfaces at 25.0, 26.0, and 26.8 $\sigma_\theta$  ( Fig. 5 ) are illustrated to examine how these  
362 trends occur and how they are connected. These density surfaces correspond to the shallower density  
363 range of Subtropical Mode Water ( STMW ), the shallower densities of Central Mode Water ( CMW )  
364 [ Suga et al., 1997; 2004 ], and the representative density of North Pacific Intermediate Water ( NPIW )  
365 [ Nakamura et al., 2000a, b; Nakamura and Awaji, 2003; Yasuda, 2004 ], respectively. STMW is  
366 formed south of the Kuroshio Extension between 30–35°N and 130–170°E, and reaches depths of  
367 approximately 400 m in late winter. It then spreads toward the subtropical front through advection  
368 across the Kuroshio recirculation area. CMW is formed in the transition area of the central North  
369 Pacific and spreads eastward along the North Pacific Current before turning southward and westward  
370 in the subtropical gyre [ Suga et al., 1997; 2004 ]. In contrast, NPIW does not outcrop during its  
371 formation process. Its origin lies in Okhotsk Sea Mode Water, which forms through overturning driven  
372 by diapycnal upwelling and tidal mixing around the Kuril Islands [ Nakamura et al., 2000a, b;  
373 Nakamura and Awaji, 2003; You, 2003; Yasuda, 2004 ] as well as double diffusions in the North Pacific  
374 [ You, 2003 ].

375

376 The linear trends on the 25.0, 26.0, and 26.8 $\sigma_\theta$  surfaces show that positive and negative tendencies  
377 appear in characteristic locations and are generally aligned with the geostrophic streamlines ( Fig. 5a–  
378 b, d–e, g–h ). Although exceptions exist, such as weak positive trends ( 150–175°E, 20–30°N ) ( Fig.  
379 5a–b ), negative trends in potential temperature and salinity dominate in the western and central North  
380 Pacific on the 25.0 and 26.0 $\sigma_\theta$  surfaces ( Fig. 5a–b, d–e ). Conversely, positive trends in temperature  
381 and salinity are most prevalent in the northeastern and/or eastern regions of the basin along the  
382 geostrophic streamlines ( Fig. 5a–b, d–e ). These patterns suggest that waters subducted in the frontal  
383 region with reduced temperature and salinity originate mainly from the northeastern North Pacific and  
384 are advected southward along the subtropical circulation ( Fig. 5a–b, d–e ). Exceptions occur in parts

385 of the northeastern basin (  $170\text{--}130^\circ\text{W}$ ,  $40\text{--}60^\circ\text{N}$  ), where warmer and more saline waters influence  
386 the water masses sinking near the Alaska gyre and subsequently transported outside the subtropical  
387 gyre and along the California coast.

388

389 At  $26.8\sigma_\theta$  ( Fig. 5g–h ), large positive trends in temperature and salinity are found along the Kuril  
390 Islands, with moderate positive trends appearing on the eastern side of the basin, respectively. Waters  
391 at this density range (  $26.8\sigma_\theta$  ) are not directly ventilated but are formed through diapycnal mixing  
392 processes [ Nakamura et al., 2000a, b; Nakamura and Awaji, 2003; You, 2003; Yasuda, 2004 ] and  
393 through double diffusion such as salt fingering [ You, 2003 ]. Thus, the observed positive temperature  
394 and salinity trends at  $26.8\sigma_\theta$  likely reflect influences from changes occurring in the overlying layers  
395 ( Fig. 5d–e and g–h ).

396

397 A meridional northward shift of the outcrop line in the North Pacific associated with recent climate  
398 change has been documented in OFES analyses [ Ogata and Nonaka, 2020 ] and in other observational,  
399 reanalysis, and eddy-resolving ocean hindcasts [ Xu et al., 2022 ]. Consistent with these studies, the  
400 present dataset exhibits clear northward migration of the  $25.0\sigma_\theta$  and  $26.0\sigma_\theta$  outcrop lines ( Fig. 6a ),  
401 with the strong shifts occurring in the eastern basin between  $150^\circ\text{E}$  and  $180^\circ\text{W}$  (Fig. 6 and Table 1).  
402 The estimated northward shift rate at  $0.004\text{--}0.09\text{ }^\circ\text{yr}^{-1}$  from 2004 to 2023 is comparable to the value of  
403  $0.04\text{ }^\circ\text{yr}^{-1}$  reported by Xu et al. [ 2022 ] for 1980 to 2018. Xu et al. [ 2022 ] further demonstrated that  
404 changes in the mixed layer and outcrop lines are tightly coupled with the northward migration of the  
405 North Pacific subtropical gyre and KE/OE fronts due to the poleward expansion of the Hadley cell,  
406 including the fact that the Kuroshio Extension and Oyashio Extension fronts, mode waters, and  
407 subtropical fronts evolve as a coherent system. These changes may also reflect the influence of  
408 anthropogenic warming, which has been linked to the poleward expansion of the Hadley circulation

409 and the associated meridional shifts of oceanic fronts [ Yang et al., 2020 ].

410

411 Such poleward displacements of frontal structures can help explain the negative temperature and  
412 salinity trends in the subtropical gyre, where less saline subarctic-origin waters are subducted and  
413 advected southward. The positive temperature and salinity trends occurring in the Alaska region  
414 [ 160°–130°W, 30°–60°N ] ( Fig. 5a–b and d–e ) are likewise consistent with the direct surface  
415 warming. In contrast, the 26.0 $\sigma_\theta$  front exhibits primarily longitudinal, rather than meridional, shifts  
416 between 2004 and 2023 ( Fig. 6 ), suggesting that the associated temperature and salinity changes arise  
417 mainly from direct surface warming and freshening, rather than from density-compensated shifts in  
418 water-mass distribution.

419

### 420 3.3.2 Dissolved oxygen

421 The linear trends in dissolved oxygen on the isopycnal surfaces at 25.0, 26.0, and 26.8 $\sigma_\theta$  exhibit  
422 predominantly negative values across the North Pacific ( Fig. 5c, f, and i ), although their spatial  
423 distributions are not uniform. Large negative trends are concentrated in the northeastern and eastern  
424 regions and gradually decrease toward the west ( Fig. 5c, f, and i ). Exceptions occur mainly in the  
425 tropics, where notable positive trends are found in the western tropical areas on the 26.0 and 26.8 $\sigma_\theta$   
426 surfaces.

427

428 The temporal changes in dissolved oxygen ( O<sub>2</sub> ) were decomposed following the method of Sasano et  
429 al. [ 2015 ]. The processes underlying the oxygen tendency equations ( Eqs. 2 and 3 ) are summarized  
430 below. We evaluated each contributing term and examined its relative importance for the dissolved O<sub>2</sub>  
431 trends. The total tendency of dissolved oxygen can be expressed as

432 
$$\frac{\partial O_2}{\partial t} = \left( \frac{\partial O_2}{\partial z} \frac{\partial z}{\partial t} \right) + \left( \frac{\partial O_2^{sat}}{\partial t} \right)_{net} - \left( \frac{\partial(AOU)}{\partial t} \right)_{net}, \quad (2)$$

433 which can be rearranged as

434 
$$\frac{\partial O_2}{\partial t} = \underbrace{\left( \frac{\partial O_2}{\partial z} \frac{\partial z}{\partial t} \right)}_{(i)} + \underbrace{\left( \frac{\partial O_2^{sat}}{\partial t} - \frac{\partial O_2^{sat}}{\partial z} \frac{\partial z}{\partial t} \right)}_{(iii)} + \underbrace{\left( -\frac{\partial(AOU)}{\partial t} + \frac{\partial(AOU)}{\partial z} \frac{\partial z}{\partial t} \right)}_{(vi)}. \quad (3)$$

435 (i) (ii) (iii) (iv) (v) (vi)

436 Here,  $X = O_2, O_2^{sat}, AOU$  ( Apparent Oxygen Utilization ). The term  $\partial z/\partial t$  denotes the temporal  
 437 change in the depth of the isopycnal surface (z), while  $\partial X/\partial z$  represents the vertical gradient of the  
 438 variable  $X$  at that surface, averaged over the past 20 years. The net tendency term  $(\partial X/\partial t)_{net}$   
 439 represents the net changes associated with a variable X.

440

441 By applying Eq. ( 3 ), the rate of  $O_2$  change ( term i ), which is the rate of reconstructed  $O_2$  data  
 442 estimated from the linear regression analysis, on each isopycnal surface can be decomposed into  
 443 contributions from:

444 ( term ii ) vertical heave acting on the vertical  $O_2$  gradient;

445 ( term iii ) solubility effects due to temperature and salinity changes;

446 ( term iv ) vertical heave acting on the solubility gradient;

447 ( term v ) AOU changes related to air-sea disequilibrium, biological activities, and lateral circulation

448 ( term vi ) vertical heave acting on AOU gradients.

449 The derivation of Eqs. ( 2 ) and ( 3 ) follows Sasano et al. [ 2015 ] and is described in Appendix. A  
 450 schematic illustration of this decomposition is provided in Supplementary Figure S5.

451

452 Figure 7 shows the horizontal distributions of the magnitude of each term on 25.0, 26.0, and 26.8 $\sigma_\theta$   
453 surfaces. The results indicate that the prominent O<sub>2</sub> declines ( Fig. 5c, f, i ) arise from a combination  
454 of positive and negative contributions, with the dominant terms varying by latitude. In the high-latitude  
455 region around the Alaska Gyre ( 170°–130°W, 40°–60°N ), the largest negative contributions are  
456 associated with the deepening of isopycnal surfaces ( term ii ) and the vertical heave acting on the  
457 AOU gradient ( term vi ) ( Fig. 7f, j, k, o ). Because the dissolved oxygen generally decreases with  
458 depth (  $\partial O_2 / \partial z < 0$  ), deepening of isopycnal surfaces (  $\partial z / \partial t > 0$  ) ( Fig. 8 b–c ) produces a  
459 negative contribution through vertical heave. Similarly, because AOU typically increases with depth,  
460 isopycnal deepening leads to an apparent increase in AOU, contributing negatively to dissolved O<sub>2</sub> via  
461 term ( vi ). In contrast, solubility-related changes ( term iii ) and net AOU tendencies ( term v ) act in  
462 opposite directions during this period ( Fig. 7g–h, l–m ). Taken together, these results are consistent  
463 with the strong negative O<sub>2</sub> trends observed in the Bering Sea on the 26.0 $\sigma_\theta$  and 26.8 $\sigma_\theta$  surfaces  
464 ( 150°E–170°W, 50–60°N; Figs. 5f and i ).

465

466 In the subtropical and mid-latitudes ( 10°–40°N ), the O<sub>2</sub> decline is largely associated with AOU  
467 changes ( term v ) ( Fig. 7d, i, and n ). The relative weakening of the total O<sub>2</sub> decrease in the western  
468 North Pacific ( Fig. 5c, f, i ) coincides with positive contributions from vertical heave of isopycnal  
469 surfaces ( term ii ) ( Fig. 7f and k ). Additional positive trends arise from solubility-related effects  
470 ( term iii ) ( Fig. 7b ), and the vertical heave acting on the AOU gradient ( term vi ) ( Fig. 7j and o and  
471 Fig. 8b–c ).

472

473 In the mid-ocean between 170°E and 160°W, the positive O<sub>2</sub> tendencies transition to weakly negative  
474 values. In contrast, a pronounced band of positive trends is found zonally across the North Pacific

475 Ocean between 30°N and 50°N, primarily associated with the combined effects of terms ( iii ) and ( v )  
476 ( Fig. 7l, h–i, and m–n ). This pattern may be related to the northward meridional shift of the subtropical  
477 and subarctic frontal zone under recent global warming [ Ogata and Nonaka, 2020 ]. Enhanced winter  
478 convection in this region may introduce nutrients into the surface layer, potentially increasing  
479 biological activity and AOU. In the NPIW formation region near the Kuril Islands, negative  
480 contributions from term ( iii ) are observed ( Fig. 7l ), suggesting weaker vertical mixing during the  
481 observational period, likely influenced by enhanced surface-layer stratification. This interpretation is  
482 supported by the positive trends in temperature and salinity observed in the winter subducted areas  
483 [ Suga et al., 1997; 2004; Yasuda, 2004 ] ( Fig. 5d–e, g–h ).

484

485 In the western tropical Pacific, pronounced increases in dissolved O<sub>2</sub> are observed within the density  
486 range of 26.8–27.2  $\sigma_\theta$  ( Fig. 3c and g; Fig. 4c and g; Fig. 5c, f, and i ), overlapping with the OML  
487 [ Reid, 1997 ]. Similar features have been reported by Sasano et al. [ 2015 ] and Takatani et al. [ 2012 ].  
488 Variability of the North Equatorial Counter Current ( NECC ) is likely relevant in this region.  
489 According to the study of Chen et al. [ 2016 ] based on the OFES outputs including a multidecadal  
490 variability (1960–2014), the NECC exhibits two distinct modes of variability: an interannual mode  
491 characterized by strengthening accompanied by southward migration, and an interdecadal mode  
492 marked by a gradual weakening, poleward migration, and broadening.

493

494 The validity of time-varying signals in the western tropical Pacific in the OFES data has been  
495 demonstrated by Chen et al. [ 2016 ]. We further examined the longer-term OFES data ( 1950–2023 ),  
496 as well, for poleward, eastward velocities, as well as potential temperature and salinity here ( Fig. 9c,  
497 g ). Positive temperature anomalies in 0°–5 °N occur above 250 m depth, while negative anomalies

498 appear along the  $26.0\sigma_\theta$  surface between  $5^\circ$ – $20^\circ$ N, a similar pattern that is also evident in the GOBAI-  
499  $O_2$  data ( Fig. 3a ). A discrepancy is found in salinity trends: GOBAI- $O_2$  shows negative trends along  
500  $26.0\sigma_\theta$  ( Fig. 3b ), whereas OFES exhibits positive trends ( Fig. 9b, f ), likely reflecting higher salinity  
501 at 200–600 m depth in OFES between  $0^\circ$  and  $7^\circ$ N ( Fig. 10b, d ).

502

503 Anomalies in poleward and eastward velocities ( Fig. 9a–b, e–f and Fig. 11a–b ) indicate enhanced  
504 poleward flow around  $5^\circ$ N above 200m depth and a poleward shift of the eastward velocity core. These  
505 changes are consistent with the interdecadal mode of NECC variability described by Chen et al.  
506 [ 2016 ]. The broadening of the NECC was less evident here, possibly because the present analysis  
507 uses raw velocity fields rather than isolating the second EOF modes. The wind-stress curl over the  
508 equatorial Pacific shows a persistent decrease and poleward expansion of negative values along the  
509  $0^\circ$ – $10^\circ$ N from 1950 to 2023 ( Fig. 12 ).

510

511 The westward penetration of the OML is slow and occurs between two eastward-extending tongues of  
512 high  $O_2$  water originating near the equator [ Reid, 1997 ] (Fig. S6). The observed  $O_2$  increase on the  
513  $26.8$ – $27.2 \sigma_\theta$  surfaces ( Fig. 3c, g and Fig. 4c, g ) is consistent with a weakening and northward shift  
514 of the interdecadal NECC mode. The subsurface  $O_2$  increase, particularly below 400m depth ( Fig. 1r–  
515 u ), is therefore likely influenced by these circulation changes, potentially allowing higher- $O_2$  water to  
516 extend westward ( Fig. S6 ). In addition, shoaling of isopycnal surfaces near the equator indicates a  
517 northward shift of the boundary between the tropical and subtropical gyres along  $137^\circ$ E line during  
518 the observational period.

519

#### 520 **4. Discussion and Conclusion**

521 The variability of dissolved oxygen in the North Pacific reflects the combined influences of global  
522 warming and climate variability. In this study, we used the four-dimensional GOBAI-O<sub>2</sub> dataset,  
523 constructed using machine-learning methods applied to historical temperature, salinity, and oxygen  
524 observations from BGC-Argo floats and ship-based measurements—to examine linear trends in  
525 potential temperature, salinity, and dissolved oxygen over the past two decades ( 2004–2023 ). The  
526 linear trends are broadly consistent with findings from previous studies [ Takatani et al. 2012; Sasano  
527 et al. 2015; Ogata and Nonaka, 2020 ], and we clarified how these trends vary spatially ( Figs. 3 and  
528 4 ).

529

530 An important outcome of this study is that GOBAI-O<sub>2</sub>, being globally gridded, allows spatially  
531 continuous and smooth representations of trends, both horizontally and vertically, across the North  
532 Pacific. This provides a more coherent picture than earlier datasets that relied solely on sparse ship-  
533 based observations. The horizontal trend patterns mapped on isopycnal surfaces ( Fig. 5 ) show that  
534 dissolved oxygen exhibits a basin-scale decreasing trend. At the same time, several regions display  
535 locally increasing oxygen, including areas influenced by the meridional migration of subtropical and  
536 subpolar fronts ( Fig. 4 ). The strong positive oxygen trends in the western equatorial region are  
537 consistent with a weakening of the second mode of the NECC variability. The decomposition analysis  
538 further illustrates how each physical component contributes to oxygen changes along isopycnal  
539 surfaces ( Fig. 7 ).

540

541 Although many of the large-scale features identified here resemble those reported by Ito et al. [ 2017 ],  
542 our analysis reveals regional and isopycnal-scale structures that were previously unresolved. In  
543 particular, the positive oxygen trends in the Kuroshio–Oyashio Transition Zone, the northeastern North

544 Pacific along the 26.8–27.0  $\sigma_\theta$  density surfaces, and the enhanced subsurface O<sub>2</sub> increase in the tropical  
545 western Pacific below 400 m were not clearly distinguished in earlier climatology-based studies. These  
546 improvements arise because GOBAI-O<sub>2</sub> integrates high-frequency BGC-Argo oxygen observations  
547 with a spatially consistent mapping scheme, reducing observational gaps and sampling biases in  
548 dynamically active regions. This demonstrates that regional reoxygenation signals can coexist with  
549 large-scale deoxygenation, and highlights the importance of sustained BGC-Argo observations for  
550 detecting emerging changes in ocean biogeochemistry.

551

552 Recent work by Bushinsky et al. [ 2025 ] has reported the presence of a systematic negative bias  
553 (approximately -2.7  $\mu\text{mol kg}^{-1}$ ) in air-calibrated BGC-Argo oxygen measurements compared with  
554 ship-based reference profiles. This bias does not appear to be explicitly corrected in the GOBAI-O<sub>2</sub>  
555 and may therefore influence the magnitude of the estimated oxygen trends—potentially enhancing  
556 negative trends or suppressing positive ones in regions with dense float sampling. However, as  
557 described in Section 2.1, a substantial fraction of these float data is subject to quality control through  
558 comparison with climatological fields derived from ship-based discrete observations, and only profiles  
559 with appropriate quality flags are retained and incorporated into the dataset development. This filtering  
560 procedure likely mitigates a portion of the air-calibration bias.

561

562 If present, such biases could also affect the apparent vertical structure of the oxycline. In the North  
563 Pacific, regions with high float density—such as the Kuroshio–Oyashio transition zone, the North  
564 American coastal region, and the vicinity of Hawaii—may be particularly affected (see Fig. 1 of Sharp  
565 et al., 2023). While a constant offset would not directly alter linear trend estimates, any time–varying  
566 bias associated with sensor behavior or sampling depth could introduce spurious trends. A quantitative  
567 evaluation is not feasible at present due to the lack of temporally continuous ship-based reference data

568 at the spatial scales. This limitation should therefore be kept in mind when interpreting the O<sub>2</sub> trends  
569 reported here.

570

571 It is also essential to recognize that GOBAI-O<sub>2</sub> is a machine learning reconstruction derived from  
572 available temperature, salinity, and oxygen measurements. While this approach significantly enhances  
573 spatial coverage, the results should be interpreted cautiously. Importantly, however, such  
574 methodological uncertainties are unlikely to alter the large-scale spatial coherence of the trend patterns  
575 identified in this study. Nevertheless, future work incorporating improved calibration of Argo oxygen  
576 sensors, expanded ship-based reference datasets, independent machine learning reconstructions [ e.g.,  
577 Ito et al., 2024 ], and comprehensive ocean reanalysis will be necessary to better constrain these  
578 uncertainties.

579

580 The monthly mean climatological GOBAI-O<sub>2</sub> data set should include the Pacific Decadal Oscillation  
581 ( PDO; Stramma et al., 2020; Pozo Buil and Di Lorenzo, 2017 ) and the North Pacific Gyre Oscillation  
582 ( NPGO; Stramma et al., 2020 ). This dataset, therefore, provides a valuable basis for examining how  
583 such climate variability influences dissolved oxygen through physical driving mechanisms.  
584 Investigating these relationships more explicitly will be an important direction for future research.

585

586

587 **Data availability:**

588 GOBAI-O<sub>2</sub> data is available at [https://www.ncei.noaa.gov/access/metadata/landing-](https://www.ncei.noaa.gov/access/metadata/landing-page/bin/iso?id=gov.noaa.nodc:0259304)  
589 [page/bin/iso?id=gov.noaa.nodc:0259304](https://www.ncei.noaa.gov/access/metadata/landing-page/bin/iso?id=gov.noaa.nodc:0259304). Temperature and salinity are from Roemmich and Gilson  
590 [ 2009] Argo climatology ( [https://sio-argo.ucsd.edu/RG\\_Climatology.html](https://sio-argo.ucsd.edu/RG_Climatology.html) ). The OFES, NCEP-  
591 NCAR, and GODAS data used in our study are obtained from APDRC, University of Hawaii  
592 ( <http://apdrc.soest.hawaii.edu> ).

593

594 **Author contributions:**

595 MI designed the study, performed the analyses, and prepared all figures. MI wrote the initial draft of  
596 the manuscript. MI and TO contributed to the interpretation of the results. All authors contributed to  
597 improving the manuscript.

598

599 **Acknowledgements:**

600 Jonathan D. Sharp and the reviewers are acknowledged for providing comments that prompted  
601 significant improvements to this manuscript.

602

603

604 **Financial support:**

605 This research has been supported by the Institute for Basic Science (grant no. IBS-R028-D1) and the  
606 Japan Society for the Promotion of Science (JSPS) through a Grant-in-Aid for Scientific Research  
607 JP22H00176.

608

609

610

611

612

613

614

615

616

617

618 **Table captions:**

619 Table 1. Northern shifts of the (outcrop) isopycnal latitudes ( $^{\circ} \text{ yr}^{-1}$ ) for  $25.0\sigma_{\theta}$  (a),  $26.0\sigma_{\theta}$  (b), and  
 620  $26.8\sigma_{\theta}$  (c) in the GOBAI-O<sub>2</sub>, OFES, and GODAS datasets. The estimates are based on data from March  
 621 of each year. For  $26.8 \sigma_{\theta}$ , the northern shift is evaluated using the isopycnal depths corresponding to  
 622 182, 178m, and 183m in GOBAI-O<sub>2</sub>, OFES, and GODAS, respectively.

623 (a)  $25.0\sigma_{\theta}$ 

<b>Longitude</b>	<b>GOBAI-O<sub>2</sub></b>	<b>OFES</b>	<b>GODAS</b>
<b>150 °E</b>	0.0241	0.0157	0.0283
<b>170 °E</b>	0.0444	0.0052	0.0240
<b>170 °W</b>	0.0684	0.0871	0.0481
<b>150 °W</b>	0.0947	0.0353	0.0313
<b>130 °W</b>	0.0420	0.0471	0.0121

624 (b)  $26.0\sigma_{\theta}$ 

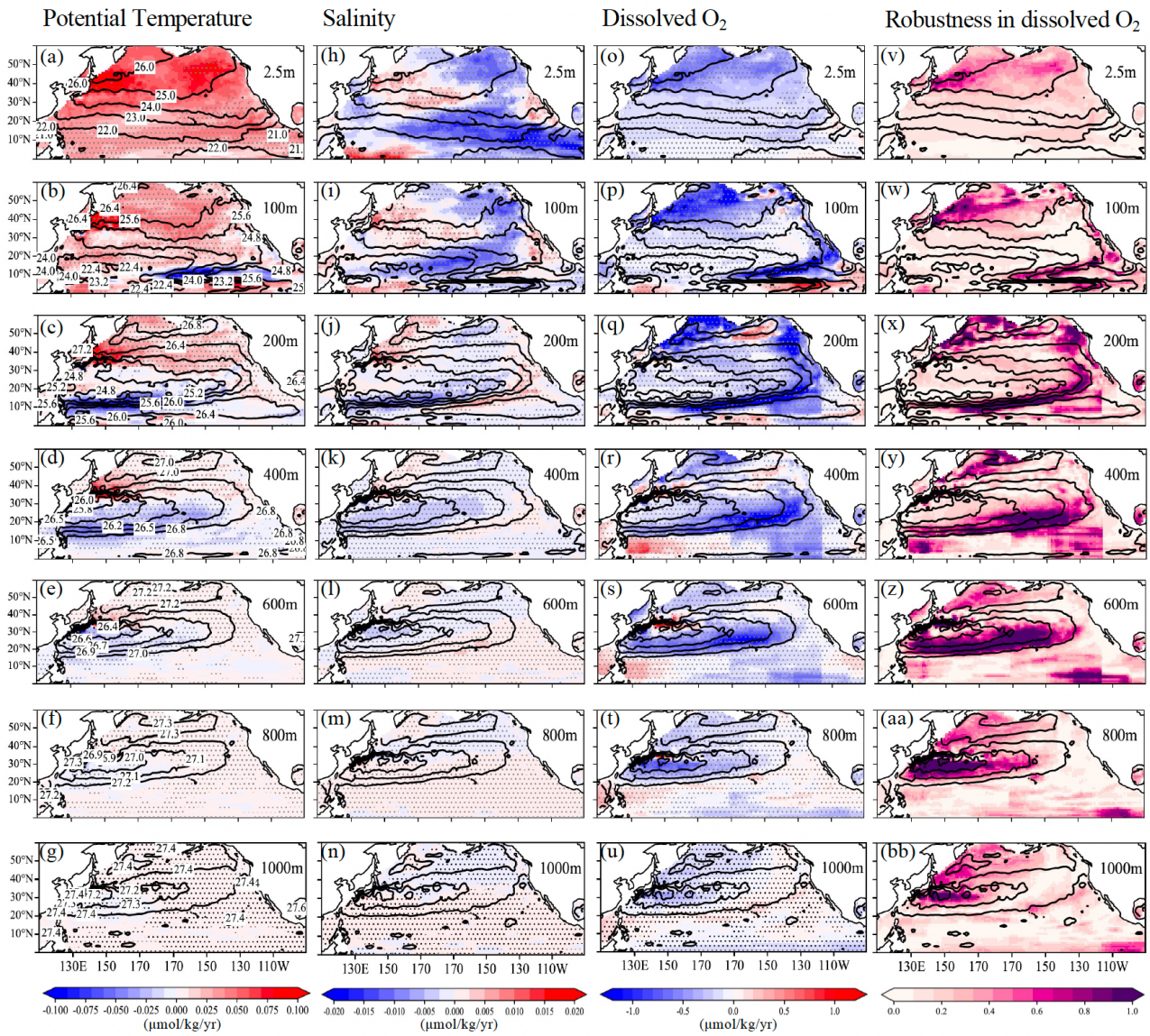
<b>Longitude</b>	<b>GOBAI-O<sub>2</sub></b>	<b>OFES</b>	<b>GODAS</b>
<b>150 °E</b>	0.0368	0.0766	0.0358
<b>170 °E</b>	0.0436	-0.0305	0.0508
<b>170 °W</b>	0.0124	0.1997	0.1412

625 (c)  $26.8\sigma_{\theta}$ 

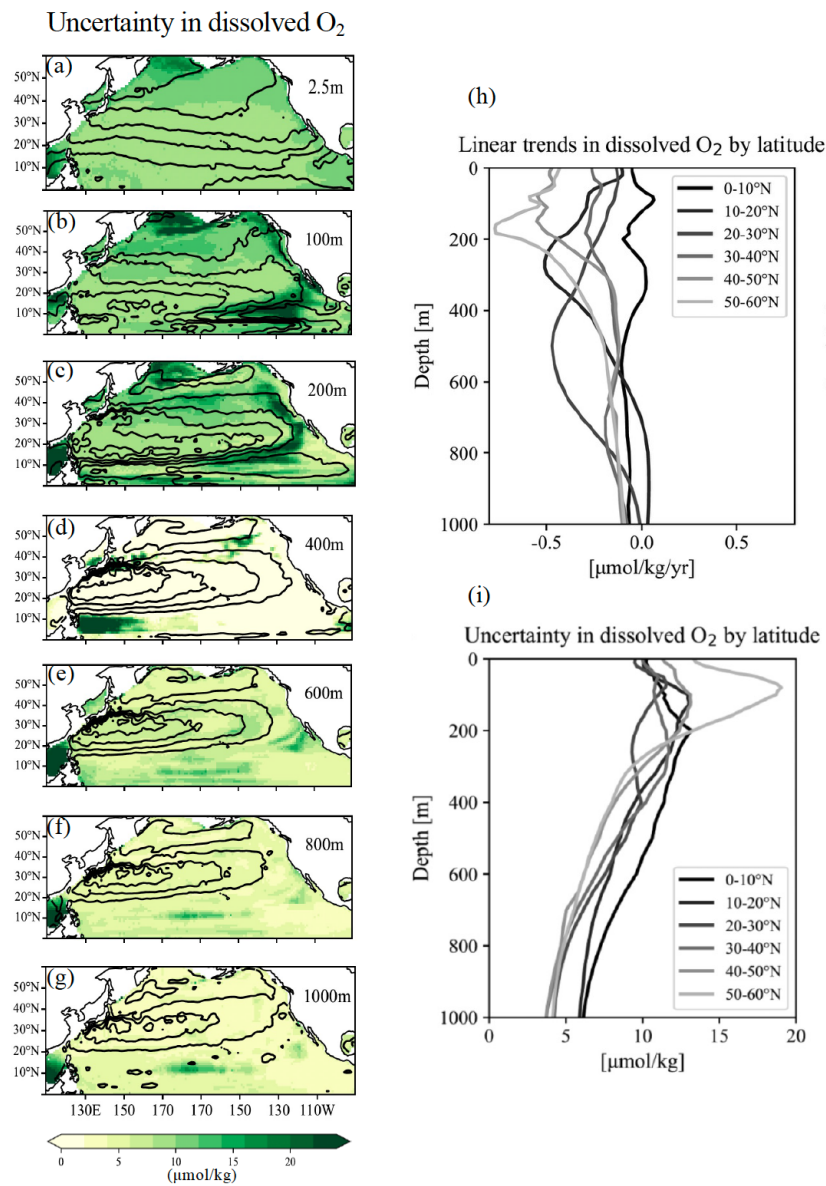
<b>Longitude</b>	<b>GOBAI-O<sub>2</sub></b>	<b>OFES</b>	<b>GODAS</b>
<b>150 °E</b>	0.0371	0.1980	0.0046
<b>170 °E</b>	0.0338	0.0217	0.1637
<b>170 °W</b>	0.0728	0.0054	0.0261

626

627



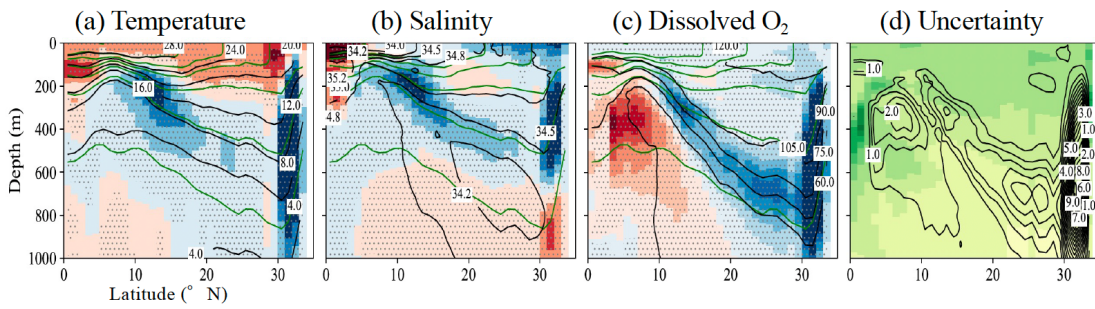
631 **Figure 1** Horizontal distributions of linear trends ( $\mu\text{mol/kg/yr}$ ) in (a–g) potential temperature, (h–  
 632 n) salinity, and (o–u) dissolved oxygen ( $\text{O}_2$ ) during the observational period at depths of 0, 100,  
 633 200, 400, 600, 800, and 1000 m, respectively. Hatched areas indicate statistically significant trends at  
 634 the 95% confidence level based on a Student’s t-test with effective degrees of freedom accounting for  
 635 temporal autocorrelation. Trend significance was evaluated using a Student’s t-test with effective  
 636 degrees of freedom accounting for lag-1 autocorrelation. Contours denote potential density at each  
 637 depth. Labels for the potential density are shown only in the potential temperature sections.  
 638 Corresponding distributions of the Robustness ( $R$ ), defined as the ratio of the trend magnitude to the  
 639 dataset uncertainty in dissolved  $\text{O}_2$  are presented in panels (v–bb).



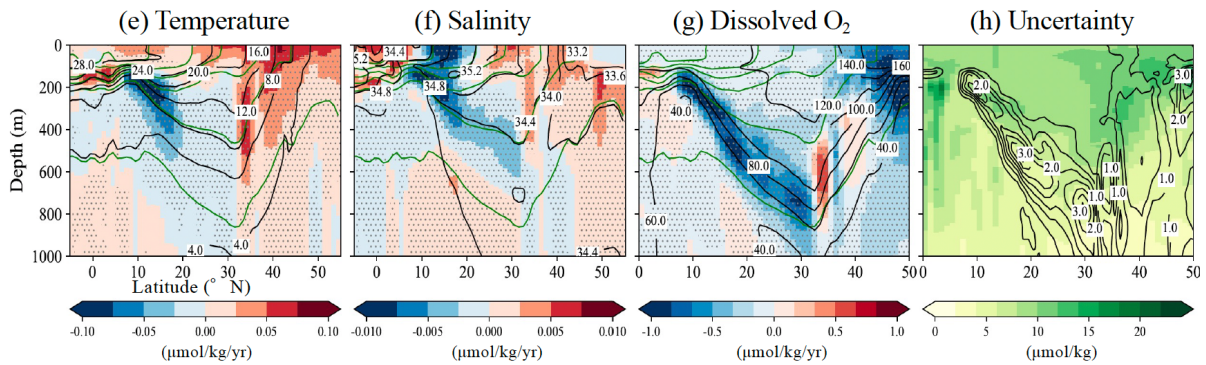
641

642 **Figure 2** Horizontal distributions of dataset uncertainty in dissolved O<sub>2</sub> ( a–g ) and vertical profiles of  
 643 linear trends and uncertainty in dissolved O<sub>2</sub> by latitude ( h–i ).

137° E line



165° E line

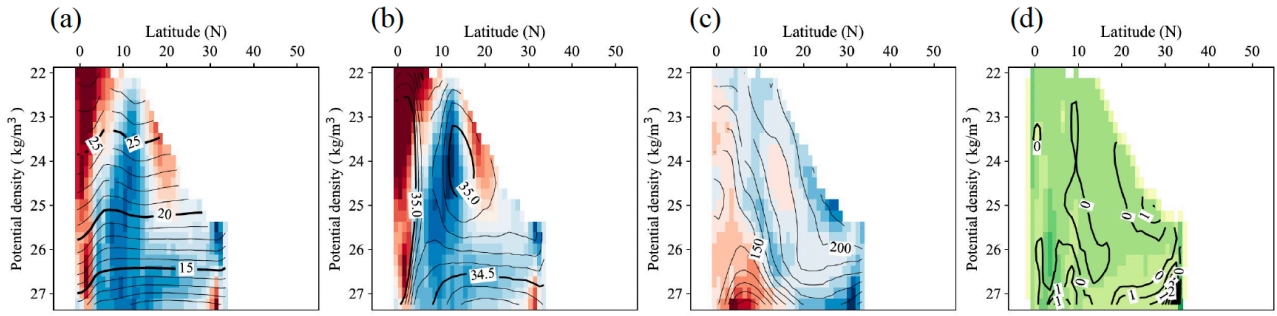


644

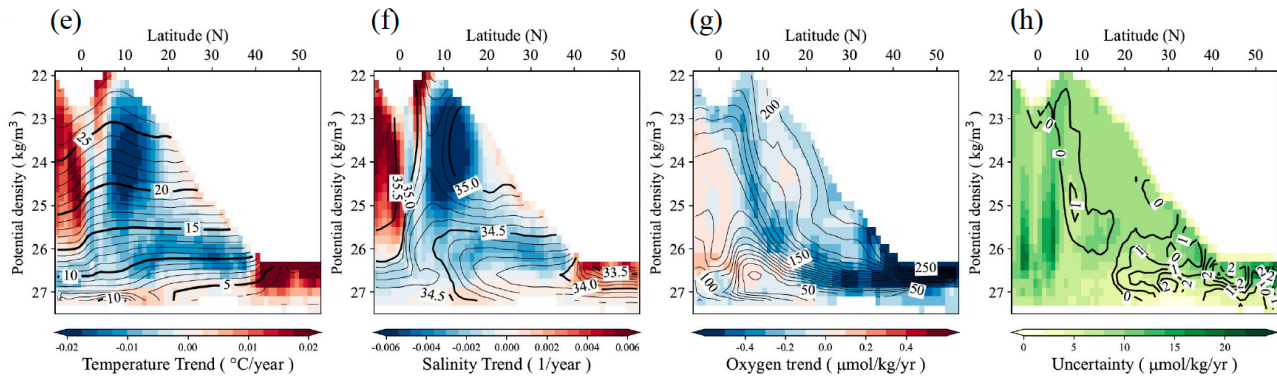
645 **Figure 3** Vertical sections showing linear trends in potential temperature ( a, e ), salinity ( b, f ), and  
 646 dissolved O<sub>2</sub> ( c, g ) along the 137°E and 165°E meridians, respectively. Black contour lines indicate  
 647 the mean potential temperature ( a, f ), salinity ( b, g ), and dissolved oxygen ( c, h ) over the period  
 648 2004–2023, while green contour lines represent the mean potential density. Labels for the potential  
 649 density are shown only in the robustness sections. Hatched areas indicate statistically significant trends  
 650 at the 95% confidence level based on a Student’s t-test with effective degrees of freedom accounting  
 651 for temporal autocorrelation. Trend significance was evaluated using a t-test with effective degrees of  
 652 freedom accounting for lag-1 autocorrelation. Corresponding vertical sections of the mean uncertainty  
 653 with the contours of the Robustness ( R ) in panels ( d, h ).

654

# 137° E Line



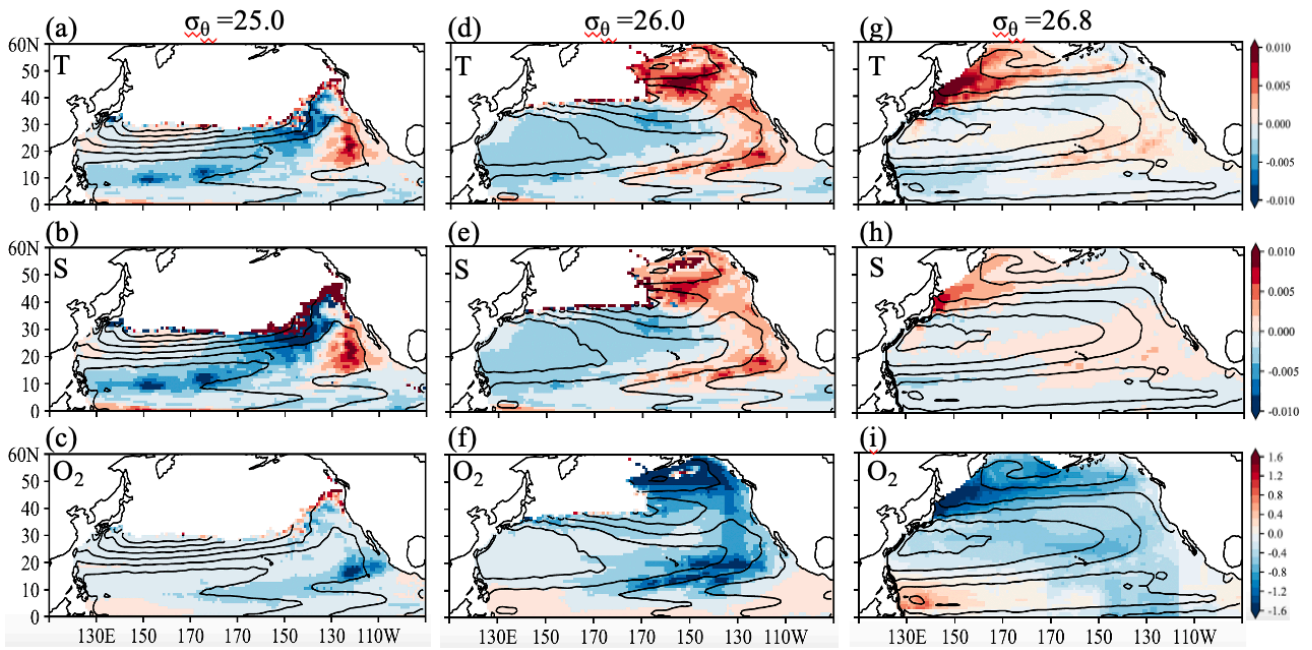
# 165° E Line



655

656 **Figure 4** Linear trends in ( a, e ) potential temperature, ( b, f ) salinity, ( c, g ), and dissolved O<sub>2</sub> on  
 657 each isopycnal surface at intervals of  $0.1\sigma_{\theta}$ , calculated at every 1.0 deg of latitude in 137 °E and 165 °E  
 658 lines, respectively. Contour lines represent the mean values during the target observation periods,  
 659 plotted at intervals of  $0.1\sigma_{\theta}$  for each 1 degree of latitude. Panels ( d, h ) show the corresponding vertical  
 660 sections of mean uncertainty, along with contours of robustness (R).

661

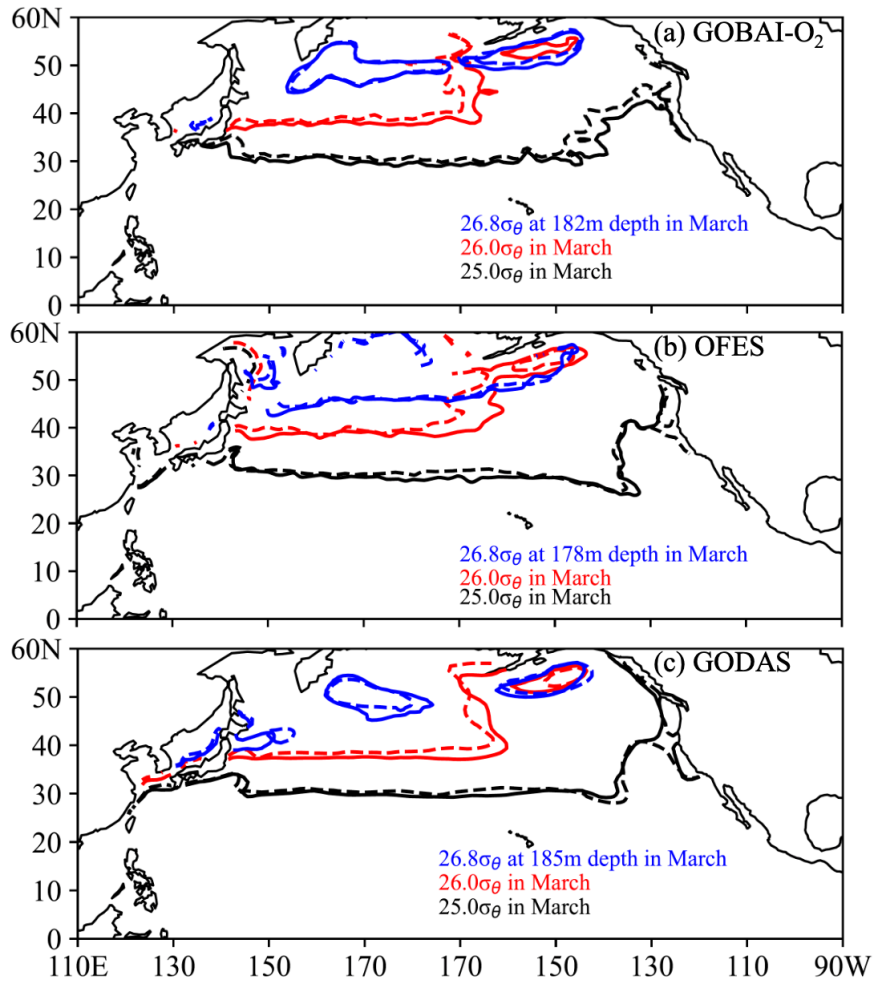


662

663 **Figure 5** Linear trends in ( a ) potential temperature, ( b ) salinity, and ( c ) dissolved O<sub>2</sub> on each  
 664 isopycnal surface at 25.0, 26.0, and 26.8σ<sub>θ</sub>. Contour lines represent geostrophic flow streamlines on  
 665 26.0 and 26.8σ<sub>θ</sub> surfaces, relative to 2000 m.

666

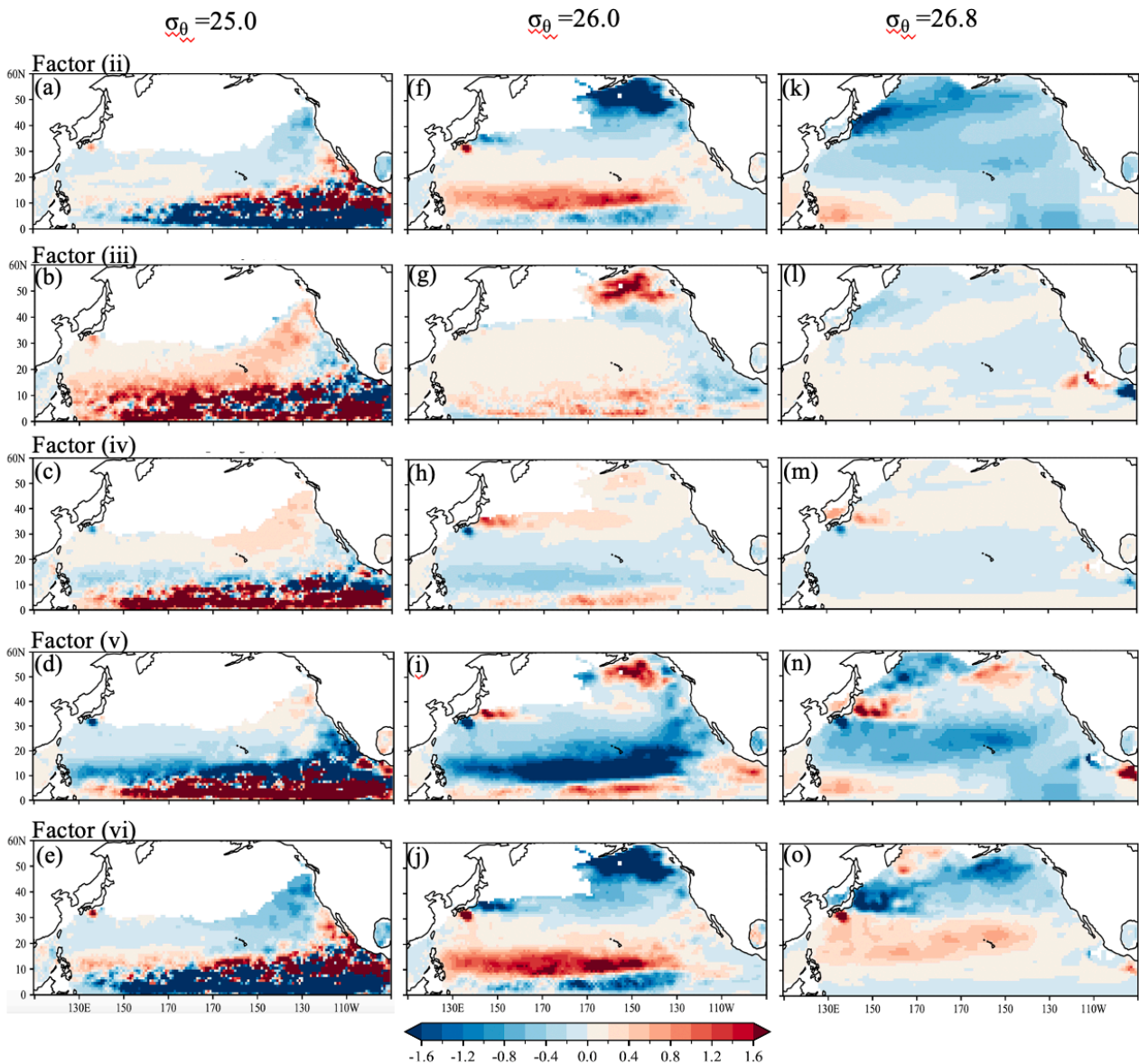
667



668

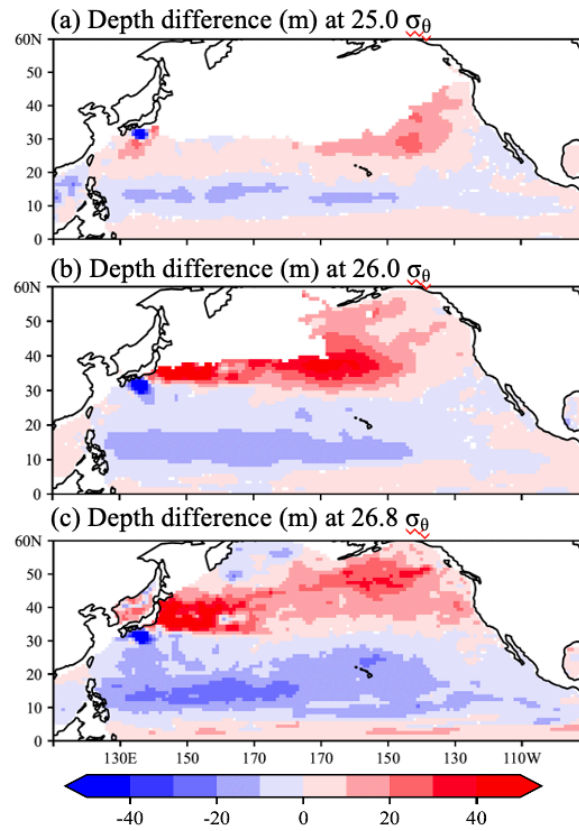
669 **Figure 6** Density contours of  $25.0\sigma_\theta$  ( black ),  $26.0\sigma_\theta$  ( red ), and  $26.8\sigma_\theta$  ( blue ) in each dataset: (a)  
 670 GOBAI-O<sub>2</sub>, (b) OFES, and (c) GODAS. Solid lines indicate the mean March density contours for  
 671 2004–2009, while dashed lines represent those for 2019–2023.

672



673

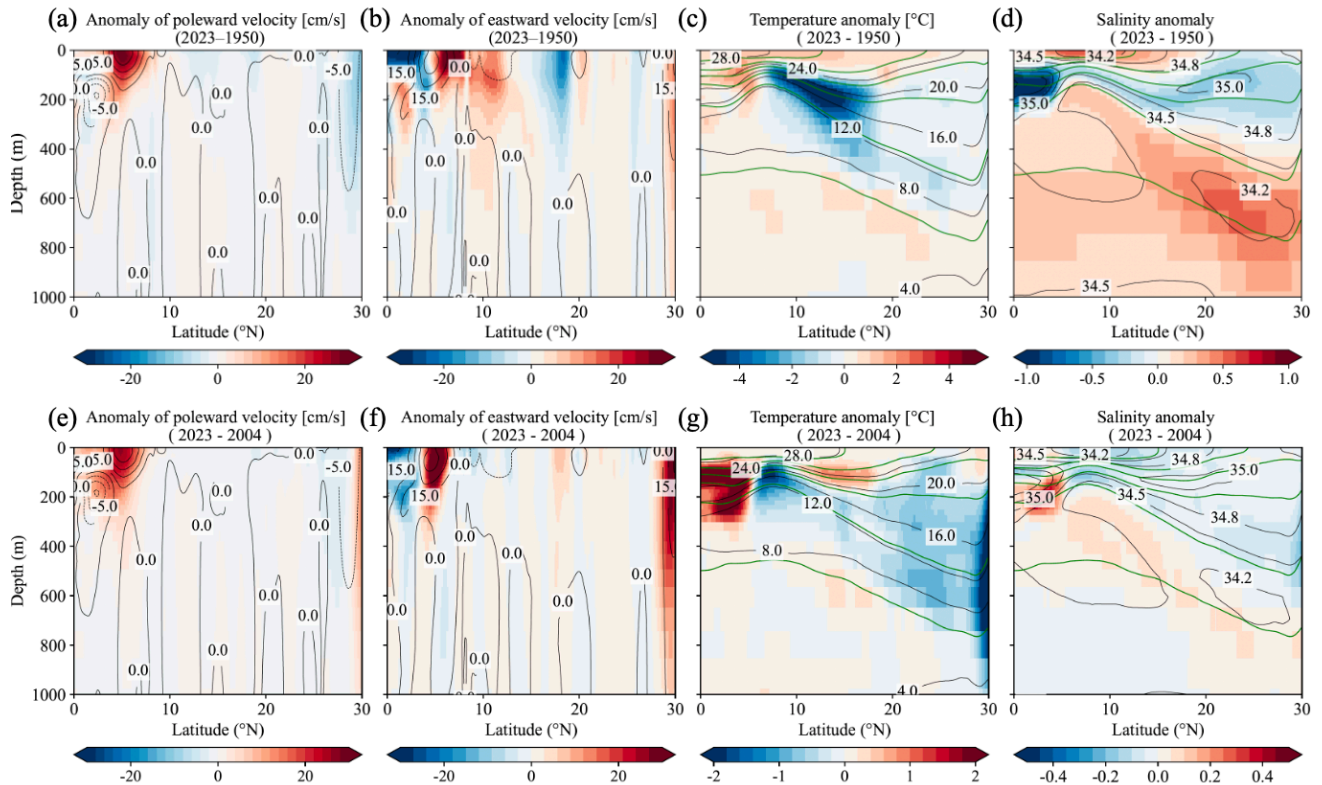
674 **Figure 7** Horizontal distributions of the magnitude of each factor contributing to the rate of  $O_2$  change  
 675 on 25.0, 26.0, and 26.8  $\sigma_\theta$  in Eq. ( 1 ). The rate of  $O_2$  change on each isopycnal surface is decomposed  
 676 into the following components: ( ii ) the apparent contribution from vertical heave (deepening or  
 677 shoaling) of isopycnal surfaces associated with warming and/or surface freshening; ( iii ) the  
 678 contribution from changes in oxygen solubility (  $O_2^{\text{sat}}$  ) associated with temperature and salinity  
 679 variations; ( iv ) the contribution from vertical heave acting on the background solubility gradient;  
 680 ( v ) the contribution from net changes in apparent oxygen utilization ( AOU ) associated with air–sea  
 681 disequilibrium, biological activity, and lateral advection and/or circulation; and ( vi ) the contribution  
 682 from vertical heave acting on AOU gradients, independent of solubility changes. This decomposition  
 683 is applied to the reconstructed dissolved oxygen fields obtained from linear regression analysis.



685

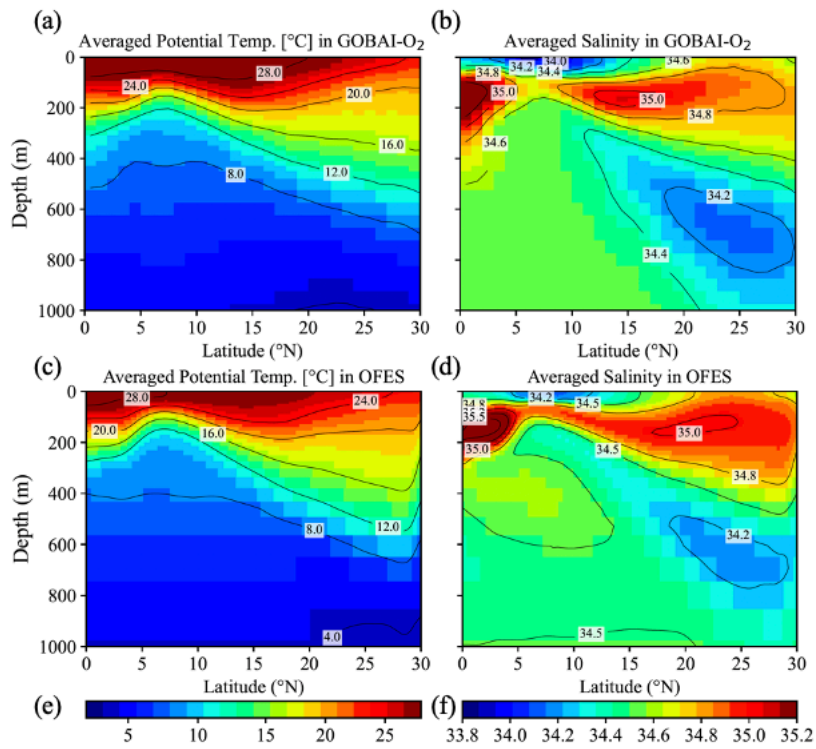
686 **Figure 8** Depth difference ( m ) between the 5-year averaged data in March, 2004–2009 and 2018–  
 687 2023 at 25.0, 26.0, and 26.8 $\sigma_{\theta}$ . The reconstructed O<sub>2</sub> data estimated from the linear regression analysis  
 688 were used in this calculation. Positive and negative values indicate the deepening and shallowing,  
 689 respectively, from the depth of each density in 2004–2023.

690



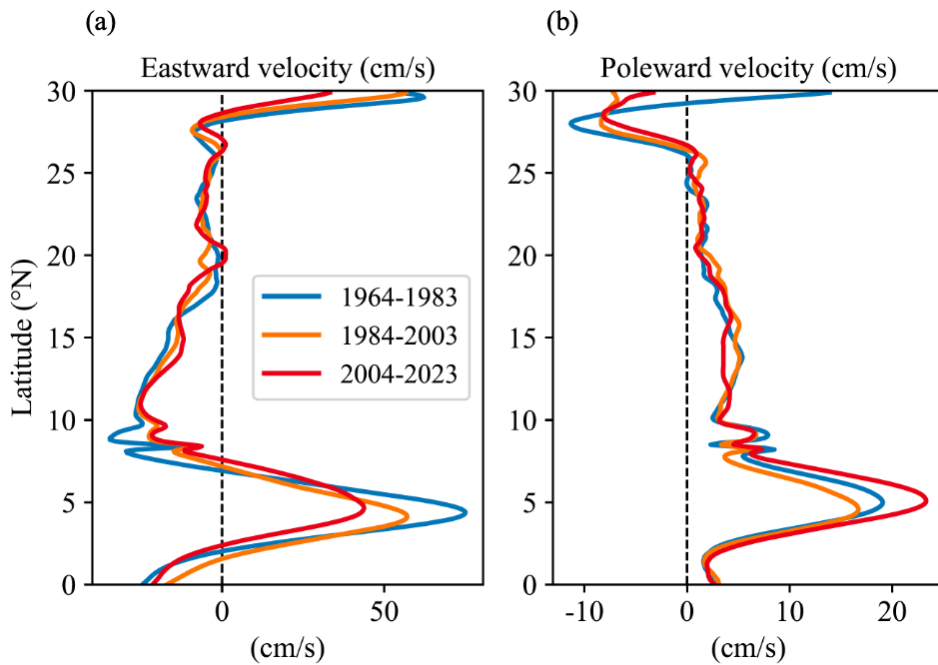
691

692 **Figure 9.** Anomaly of poleward and eastward velocity, potential temperature, and salinity in the OFES  
 693 model outputs from 1950 to 2023 ( a–d ) and from 2004 to 2023 ( e–h ), respectively, in the 137°E line.  
 694 Contours of averaged values of poleward and eastward velocity, potential temperature, and salinity  
 695 during the target period are also shown in each figure. Green contour lines in ( c–d, g–h ) indicate the  
 696 average potential density of 22, 23, 24, 25, 26, and 27 $\sigma_{\theta}$ , during the target periods.



697

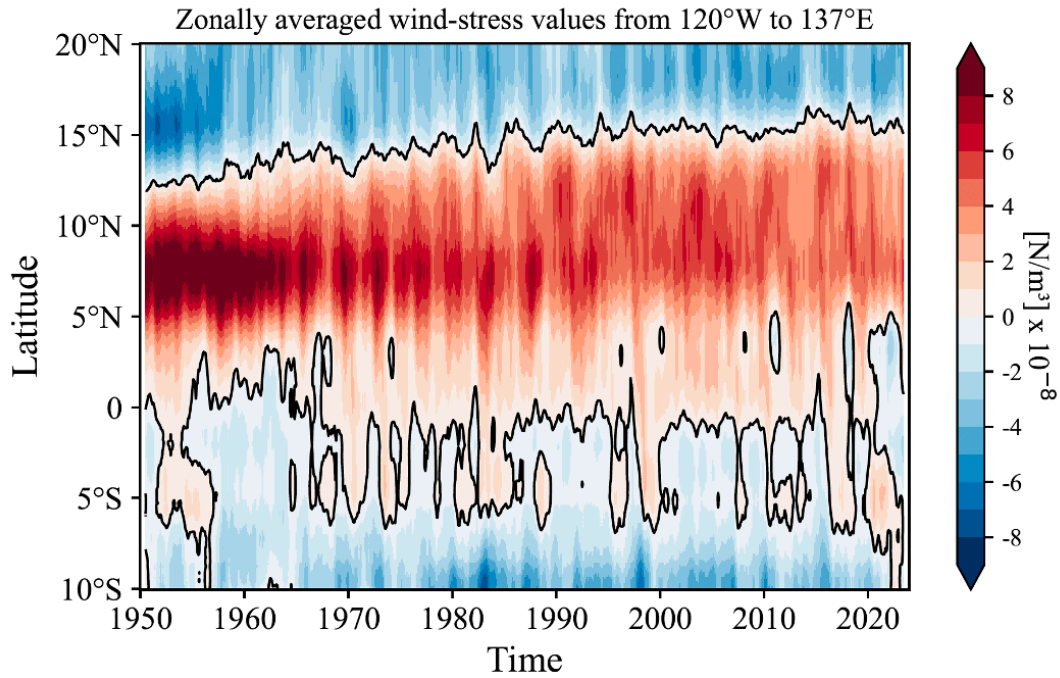
698 **Figure 10.** Averaged Potential Temperature ( a, c ) and salinity ( b, d ) in GOBAl-O<sub>2</sub> from 2004 to  
 699 2023 and OFES data from 1950 to 2023, respectively, in the 137°E line.



700

701 **Figure 11.** Latitudinal distribution of averaged eastward ( a ) and poleward velocity ( b ) in the OFES  
 702 data from 1964 to 1983, from 1984 to 2003, and from 2004 to 2023, respectively, in the 137°E line.

703



704

705 **Figure 12.** NCEP-NCAR wind-stress curl values zonally averaged from 137°E to 120° W from 1950  
 706 to 2023. A 13-month running-mean filter has been applied in time.

707

708 **Appendix: Essential concepts and derivations for Equation ( 2–3 )**

709 The essential concepts and derivations for equations ( 2 ) and ( 3 ) were originally proposed by Takatani  
 710 et al. [ 2012 ] and subsequently described in detail by Sasano et al. [ 2015 ]. Here, we briefly summarize  
 711 and follow their derivation.

712

713 When the temperature at a depth  $z_A$  increases from  $\theta_A$  to  $\theta_A'$  as a result of increased ocean heat  
 714 content, the density at that depth decreases from  $\sigma_A$  to  $\sigma_A'$ . For simplicity, the vertical salinity profile  
 715 is assumed to remain unchanged with time. As a consequence, the isopycnal surface of  $\sigma_A$  deepens  
 716 from  $z_A$  to  $z_B$  ( Figure S5 ). If surface freshening occurs simultaneously due to a net freshwater input,  
 717 both the density decreases at  $z_A$  ( from  $\sigma_A$  to  $\sigma_A'$  ) and the deepening of the isopycnal surface ( from  
 718  $z_A$  to  $z_B$  ) are enhanced. Because density is a function of temperature and salinity (  $\sigma = f(\theta, S)$  ), the

719 density of the isopycnal surface  $\sigma_A$  can be expressed as

720 
$$\sigma_A = f(\theta_A, S_A) \quad (\text{before warming}) \quad (\text{C1})$$

721 
$$= f(\theta_B', S_B). \quad (\text{after warming}) \quad (\text{C2})$$

722 Here,  $S_A$  and  $S_B$  denote salinity at depth  $z_A$  and  $z_B$ , respectively, and  $\theta_B'$  represents the temperature at  
723 density  $\sigma_A$  at depth  $z_B$  after warming. The depth  $z_B$  is determined by satisfying Eqs. (C1) and (C2).  
724 In the region where salinity decreases with depth ( e.g., above the salinity minimum layer of NPIW ),  
725  $S_A > S_B$ , and therefore  $\theta_A > \theta_B'$ . This implies that the potential temperature on an isopycnal surface  
726 effectively decreases as a consequence of warming, and that biogeochemical properties on the same  
727 isopycnal surface are also expected to change.

728

729 For a tracer  $X$  whose vertical profile with respect to depth does not change with time ( e.g., salinity;  
730 see Figure S5 ( c ) ), the temporal change of  $X$  on the potential density surface  $\sigma_A$  is attributed solely  
731 to the apparent change caused by the deepening of the isopycnal surface from  $z_A$  to  $z_B$ :

732 
$$\frac{\partial X}{\partial t} = \left( \frac{\partial X}{\partial z} \cdot \frac{\partial z}{\partial t} \right) \quad (\text{C3})$$

733 Here,  $\partial X/\partial t$  represents the temporal change of  $X$  observed on  $\sigma_A$  ( gray arrows in Figure S5 ),  $z$   
734 denotes the depth of  $\sigma_A$ ,  $\partial X/\partial z$  is the vertical gradient of  $X$  with respect to the depth ( assumed to be  
735 time-invariant ), and  $\partial z/\partial t$  is the rate of deepening of the isopycnal surface  $\sigma_A$ . The product  
736  $\partial X/\partial z \cdot \partial z/\partial t$  represents the effect of isopycnal deepening ( white arrows in Figure S5 ),  
737 corresponding to the difference between the filled square and filled circle.

738

739 For a variable  $Y$  whose vertical profile evolves with time while warming occurs simultaneously, the  
740 temporal change of  $Y$  on the density surface  $\sigma_A$  can be expressed as the sum of two components: the  
741 contribution due to the isopycnal deepening from  $z_A$  to  $z_B$  and the net temporal change of  $Y$ ,

742  $(\partial Y/\partial t)_{net}$  between the time before and after warming:

743 
$$\frac{\partial Y}{\partial t} = \left( \frac{\partial Y}{\partial z} \cdot \frac{\partial z}{\partial t} \right) + \left( \frac{\partial Y}{\partial t} \right)_{net} \quad (C4)$$

744 To evaluate the net change  $(\partial Y/\partial z)_{net}$  ( illustrated by the blue arrows of a difference in symbols  
745 between filled square and open square in Figure S5 ), it is necessary to evaluate the contribution of the  
746 temporal change of  $Y$  due to the isopycnal deepening and to subtract it from the change of  $Y$  observed  
747 at density  $\sigma_A$ . For instance, the change of  $O_2^{sat}$  in Figure S5 ( f ) is observed along the gray isopycnal  
748 surface ( large white arrow ), whereas the net change ( large blue and pink arrows ) is obtained as the  
749 difference between the observed change and the deepening effect.

750

751 The dissolved oxygen concentration  $O_2$  can be expressed as:

752 
$$O_2 = O_2^{sat} - AOU, \quad (C5)$$

753 where  $O_2^{sat}$  is the oxygen saturation concentration ( a function of temperature and salinity ), and AOU  
754 is “apparent oxygen utilization”, representing the oxygen consumed by biological processes since  
755 subduction. Near the surface, AOU is typically small, and its contributions can be neglected.

756

757 Following Eq. ( C4 ), the temporal change of  $O_2$  on a given isopycnal surface at a fixed station is:

758 
$$\frac{\partial O_2}{\partial t} = \left( \frac{\partial O_2}{\partial z} \cdot \frac{\partial z}{\partial t} \right) + \left( \frac{\partial O_2}{\partial t} \right)_{net}. \quad (C6)$$

759 Similarly,

760 
$$\frac{\partial O_2^{sat}}{\partial t} = \left( \frac{\partial O_2^{sat}}{\partial z} \cdot \frac{\partial z}{\partial t} \right) + \left( \frac{\partial O_2^{sat}}{\partial t} \right)_{net}, \quad (C7)$$

761 and

762 
$$\frac{\partial AOU}{\partial t} = \left( \frac{\partial(AOU)}{\partial z} \cdot \frac{\partial z}{\partial t} \right) + \left( \frac{\partial(AOU)}{\partial t} \right)_{net}. \quad (C8)$$

763 The term  $\text{net}$  is directly related to warming, because depends on temperature and salinity. If AOU does  
 764 not change with time, that is, if changes in  $O_2$  arise solely from changes in, then  $\partial(AOU)/\partial t$  follows  
 765 Eq. ( C3 ) and  $= 0$ . If AOU varies with time, however,  $\partial(AOU)/\partial t$  follows Eq. ( C4 ) and  $\neq 0$ , as  
 766 illustrated by the dashed gray line in Figure S5 ( g ).

767

768 Because  $O_2$  is defined by Eq. ( C5 ), the net temporal change of  $O_2$  on an isopycnal surface is

$$769 \quad \left(\frac{\partial O_2}{\partial t}\right)_{net} = \left(\frac{\partial O_2^{sat}}{\partial t}\right)_{net} - \left(\frac{\partial(AOU)}{\partial t}\right)_{net}. \quad (C9)$$

770 Combining Eqs. ( C6 ) and ( C9 ), the total temporal change of  $O_2$  on an isopycnal surface can be  
 771 written as

$$772 \quad \left(\frac{\partial O_2}{\partial t}\right) = \left(\frac{\partial O_2}{\partial z} \cdot \frac{\partial z}{\partial t}\right) + \left(\frac{\partial O_2^{sat}}{\partial t}\right)_{net} - \left(\frac{\partial(AOU)}{\partial t}\right)_{net}, \quad (C10)$$

773 which corresponds to Eq. ( 1 ) in the main text. Eq. ( C10 ) corresponds to an arrow in Figure S5 ( e ),  
 774 represented from left to right by the large gray arrow, white, blue, and pink arrows. The large blue  
 775 arrow is identical to Figure S5 ( f ), while the large pink arrow corresponds to Figure S5(g), but with  
 776 its direction reversed. Finally, substituting Eqs. ( C7 ) and ( C8 ) into ( C10 )

$$777 \quad \frac{\partial O_2}{\partial t} = \underbrace{\left(\frac{\partial O_2}{\partial z} \frac{\partial z}{\partial t}\right)}_{(i)} + \underbrace{\left(\frac{\partial O_2^{sat}}{\partial t} - \frac{\partial O_2^{sat}}{\partial z} \frac{\partial z}{\partial t}\right)}_{(ii)} - \underbrace{\left(\frac{\partial(AOU)}{\partial t} - \frac{\partial(AOU)}{\partial z} \frac{\partial z}{\partial t}\right)}_{(iii)}, \quad (C11)$$

778 ( i) ( ii) ( iii) ( iv) ( v) ( vi)

779 which corresponds to Eq. ( 2 ) in the main text. Note: The signs in terms ( v ) and ( vi ) in Eq. ( 3 ) are  
 780 reversed relative to those in Eq. ( C11 ) for convenience.

781

782 Table A1 The physical interpretation of each term in the oxygen tendency decomposition shown in Eq.  
 783 ( 3 ) and Eq. ( C11 ) is summarized.

Term	Mathematical form	Physical interpretation
(ii)	$(\partial O_2 / \partial z)(\partial z / \partial t)$	Vertical heave acting on the O <sub>2</sub> gradient
(iii)	$\partial O_2^{sat} / \partial t$	Solubility effect due to temperature and salinity changes
(iv)	$-(\partial O_2^{sat} / \partial z)(\partial z / \partial t)$	Vertical heave acting on the solubility gradient
(v)	$\partial AOU / \partial t$	AOU changes related to air–sea disequilibrium, biological activity and lateral circulation
(vi)	$-(\partial AOU / \partial z)(\partial z / \partial t)$	Vertical heave of the AOU gradient

784

785

786 **References:**

- 787 Alkire, M. B., D'Asaro, E., Lee, C., Jane Perry, M., Gray, A., Cetinić, I., et al. (2012). Estimates of  
788 net community production and export using high-resolution, Lagrangian measurements of O<sub>2</sub>, NO<sub>3</sub><sup>-</sup>,  
789 and POC through the evolution of a spring diatom bloom in the North Atlantic. *Deep Sea Research*  
790 *Part I: Oceanographic Research Papers*, 64, 157–174. <https://doi.org/10.1016/j.dsr.2012.01.012>
- 791 Behringer, D. W., & Xue, Y. (2004). Evaluation of the global ocean data assimilation system at NCEP:  
792 The Pacific Ocean. 8<sup>th</sup> Symposium on Integrated Observing and Assimilation Systems for Atmosphere,  
793 Oceans, and Land Surface, AMS 84<sup>th</sup> Annual Meeting, Washington State Convention and Trade Center,  
794 Seattle, Washington, 11-15. <https://ams.confex.com/ams/pdfpapers/70720.pdf>
- 795 Behringer, D. W. (2007). The Global Ocean Data Assimilation System (GODAS) at NCEP. 11th  
796 Symp. on Integrated Observing and Assimilation Systems for Atmosphere, Oceans, and Land  
797 Surface, San Antonio, TX, Amer. Meteor. Soc., 3.3. [Available online  
798 at <https://ams.confex.com/ams/pdfpapers/119541.pdf>.]
- 799 Berman-Frank, I., Lundgren, P., & Falkowski, P. (2003). Nitrogen fixation and photosynthetic oxygen  
800 evolution in cyanobacteria. *Research in Microbiology*, 154(3), 157–164.  
801 [https://doi.org/10.1016/S0923-2508\(03\)00029-9](https://doi.org/10.1016/S0923-2508(03)00029-9)

802 Bittig, H. C., Fiedler, B., Scholz, R., Krahnemann, G., & Körtzinger, A. (2014). Time response of oxygen  
803 optodes on profiling platforms and its dependence on flow speed and temperature. *Limnology and*  
804 *Oceanography: Methods*, 12(8), 617–636. <https://doi.org/10.4319/lom.2014.12.617>

805 Bittig, H. C., & Körtzinger, A. (2015). Tackling Oxygen Optode Drift: Near-Surface and In-Air  
806 Oxygen Optode Measurements on a Float Provide an Accurate in Situ Reference.  
807 <https://doi.org/10.1175/JTECH-D-14-00162.1>

808 Bittig, H. C., Körtzinger, A., Neill, C., van Ooijen, E., Plant, J. N., Hahn, J., et al. (2018a). Oxygen  
809 Optode Sensors: Principle, Characterization, Calibration, and Application in the Ocean. *Frontiers in*  
810 *Marine Science*, 4. <https://doi.org/10.3389/fmars.2017.00429>

811 Bittig, H. C., Steinhoff, T., Claustre, H., Fiedler, B., Williams, N. L., Sauzède, R., et al. (2018b). An  
812 Alternative to Static Climatologies: Robust Estimation of Open Ocean CO<sub>2</sub> Variables and Nutrient  
813 Concentrations From T, S, and O<sub>2</sub> Data Using Bayesian Neural Networks. *Frontiers in Marine Science*,  
814 5. <https://doi.org/10.3389/fmars.2018.00328>

815 Bopp, L., Resplandy, L., Orr, J. C., Doney, S. C., Dunne, J. P., Gehlen, M., et al. (2013). Multiple  
816 stressors of ocean ecosystems in the 21st century: projections with CMIP5 models. *Biogeosciences*,  
817 10(10), 6225–6245. <https://doi.org/10.5194/bg-10-6225-2013>

818 Boyer, T. P., and S. Levitus (1997), Objective Analyses of Temperature and Salinity for the World  
819 Ocean on a 1/48 Grid, vol. 11, NOAA Atlas NESDIS, Natl. Oceanic and Atmos. Admin., Silver Spring,  
820 Md.

821 Boyer, T. P., Antonov, J. I., Baranova, O. K., Coleman, C., Garcia, H. E., Grodsky, A., et al. (2013).  
822 World Ocean Database 2013. Retrieved from  
823 <https://repository.oceanbestpractices.org/handle/11329/357>

824 Breiman, L. (2001). Random Forests. *Machine Learning*, 45(1), 5–32.  
825 <https://doi.org/10.1023/A:1010933404324>

826 Breitburg, D., Levin, L. A., Oschlies, A., Grégoire, M., Chavez, F. P., Conley, D. J., et al. (2018).  
827 Declining oxygen in the global ocean and coastal waters. *Science*, 359(6371), eaam7240.  
828 <https://doi.org/10.1126/science.aam7240>

829 Bushinsky, S. M., Emerson, S. R., Riser, S. C., & Swift, D. D. (2016). Accurate oxygen measurements  
830 on modified Argo floats using in situ air calibrations. *Limnology and Oceanography: Methods*, 14(8),  
831 491–505. <https://doi.org/10.1002/lom3.10107>

832 Bushinsky, S.M., Nachod, Z., Fassbender, A.J., Tamsitt, V., Takeshita, Y., Williams, N., 2025. Offset  
833 Between Profiling Float and Shipboard Oxygen Observations at Depth Imparts Bias on Float pH and  
834 Derived pCO<sub>2</sub>. *Global Biogeochemical Cycles* 39, e2024GB008185.  
835 <https://doi.org/10.1029/2024GB008185>

836 Chen, X., Qiu, B., Du, Y., Chen, S., & Qi, Y. (2016). Interannual and interdecadal variability of the  
837 North Equatorial Countercurrent in the Western Pacific. *Journal of Geophysical Research: Oceans*,  
838 121(10), 7743–7758. <https://doi.org/10.1002/2016JC012190>

839 Claustre, H., Johnson, K. S., & Takeshita, Y. (2020). Observing the Global Ocean with  
840 Biogeochemical-Argo. *Annual Review of Marine Science*, 12(Volume 12, 2020), 23–48.  
841 <https://doi.org/10.1146/annurev-marine-010419-010956>

842 D’Asaro, E. A., & McNeil, C. (2013). Calibration and Stability of Oxygen Sensors on Autonomous  
843 Floats. <https://doi.org/10.1175/JTECH-D-12-00222.1>

844 Drucker, R., & Riser, S. C. (2016). In situ phase-domain calibration of oxygen Optodes on profiling  
845 floats. *Methods in Oceanography*, 17, 296–318. <https://doi.org/10.1016/j.mio.2016.09.007>

846 Estapa, M. L., Feen, M. L., & Breves, E. (2019). Direct Observations of Biological Carbon Export  
847 From Profiling Floats in the Subtropical North Atlantic. *Global Biogeochemical Cycles*, 33(3), 282–  
848 300. <https://doi.org/10.1029/2018GB006098>

849 Giglio, D., Lyubchich, V., & Mazloff, M. R. (2018). Estimating Oxygen in the Southern Ocean Using  
850 Argo Temperature and Salinity. *Journal of Geophysical Research: Oceans*, 123(6), 4280–4297.  
851 <https://doi.org/10.1029/2017JC013404>

852 Helm, K. P., Bindoff, N. L., & Church, J. A. (2011). Observed decreases in oxygen content of the  
853 global ocean. *Geophysical Research Letters*, 38(23). <https://doi.org/10.1029/2011GL049513>

854 Ito, T., Minobe, S., Long, M. C., & Deutsch, C. (2017). Upper ocean O<sub>2</sub> trends: 1958–2015.  
855 *Geophysical Research Letters*, 44(9), 4214–4223. <https://doi.org/10.1002/2017GL073613>

856 Ito, T., Cervania, A., Cross, K., Ainchwar, S., & Delawalla, S. (2024). Mapping Dissolved Oxygen  
857 Concentrations by Combining Shipboard and Argo Observations Using Machine Learning Algorithms.  
858 *Journal of Geophysical Research: Machine Learning and Computation*, 1(3), e2024JH000272.  
859 <https://doi.org/10.1029/2024JH000272>

860 Johnson, K. S., Plant, J. N., Riser, S. C., & Gilbert, D. (2015). Air Oxygen Calibration of Oxygen  
861 Optodes on a Profiling Float Array. <https://doi.org/10.1175/JTECH-D-15-0101.1>

862 Johnson, K. S., Plant, J. N., Coletti, L. J., Jannasch, H. W., Sakamoto, C. M., Riser, S. C., et al. (2017).  
863 Biogeochemical sensor performance in the SOCCOM profiling float array. *Journal of Geophysical*  
864 *Research: Oceans*, 122(8), 6416–6436. <https://doi.org/10.1002/2017JC012838>

865 Johnson, K. S., & Bif, M. B. (2021). Constraint on net primary productivity of the global ocean by  
866 Argo oxygen measurements. *Nature Geoscience*, 14(10), 769–774. [https://doi.org/10.1038/s41561-](https://doi.org/10.1038/s41561-021-00807-z)  
867 [021-00807-z](https://doi.org/10.1038/s41561-021-00807-z)

868 Kalnay, E., Kanamitsu, M., Kistler, R., Collins, W., Deaven, D., Gandin, L., et al. (1996). The  
869 NCEP/NCAR 40-Year Reanalysis Project. Retrieved from  
870 [https://journals.ametsoc.org/view/journals/bams/77/3/1520-](https://journals.ametsoc.org/view/journals/bams/77/3/1520-0477_1996_077_0437_tnyrp_2_0_co_2.xml)  
871 [0477\\_1996\\_077\\_0437\\_tnyrp\\_2\\_0\\_co\\_2.xml](https://journals.ametsoc.org/view/journals/bams/77/3/1520-0477_1996_077_0437_tnyrp_2_0_co_2.xml)

872 Kara, A. B., Rochford, P. A., & Hurlburt, H. E. (2000). An optimal definition for ocean mixed layer  
873 depth. *Journal of Geophysical Research: Oceans*, *105*(C7), 16803–16821.  
874 <https://doi.org/10.1029/2000JC900072>

875 Keeling, R. F., Körtzinger, A., & Gruber, N. (2010). Ocean Deoxygenation in a Warming World.  
876 *Annual Review of Marine Science*, *2* (Volume 2, 2010), 199–229.  
877 <https://doi.org/10.1146/annurev.marine.010908.163855>

878 Kolodziejczyk, N., Portela, E., Thierry, V., & Prigent, A. (2024). ISASO2: recent trends and regional  
879 patterns of ocean dissolved oxygen change. *Earth System Science Data*, *16*(11), 5191–5206.  
880 <https://doi.org/10.5194/essd-16-5191-2024>

881 Körtzinger, A., Schimanski, J., & Send, U. (2005). High Quality Oxygen Measurements from Profiling  
882 Floats: A Promising New Technique. <https://doi.org/10.1175/JTECH1701.1>

883 Kwiatkowski, L., Torres, O., Bopp, L., Aumont, O., Chamberlain, M., Christian, J. R., et al. (2020).  
884 Twenty-first century ocean warming, acidification, deoxygenation, and upper-ocean nutrient and  
885 primary production decline from CMIP6 model projections. *Biogeosciences*, *17*(13), 3439–3470.  
886 <https://doi.org/10.5194/bg-17-3439-2020>

887 Lauvset, S. K., Lange, N., Tanhua, T., Bittig, H. C., Olsen, A., Kozyr, A., et al. (2022b).  
888 GLODAPv2.2022: the latest version of the global interior ocean biogeochemical data product. *Earth*  
889 *System Science Data*, *14*(12), 5543–5572. <https://doi.org/10.5194/essd-14-5543-2022>

890 Li, C., Huang, Jianping, Ding, L., Liu, X., Yu, H., Huang, Jiping, 2020. Increasing Escape of Oxygen  
891 From Oceans Under Climate Change. *Geophysical Research Letters* *47*, e2019GL086345.  
892 <https://doi.org/10.1029/2019GL086345>

893 Limburg, K. E., Breitburg, D., Swaney, D. P., & Jacinto, G. (2020). Ocean Deoxygenation: A Primer.  
894 *One Earth*, *2*(1), 24–29. <https://doi.org/10.1016/j.oneear.2020.01.001>

895 Masumoto, Y., Sasaki, H., Kagimoto, T., Komori, N., Ishida, A., Sasai, Y., et al. (2004). A fifty-year  
896 eddy-resolving simulation of the world ocean: Preliminary outcomes of OFES (OGCM for the Earth

897 Simulator). *Journal of the Earth Simulator*, 1,35–56. [https://www.jamstec.](https://www.jamstec.go.jp/ceist/j/publication/journal/jes_vol.1/pdf/JES1-3.2-masumoto.pdf)  
898 [go.jp/ceist/j/publication/journal/jes\\_vol.1/pdf/JES1-3.2-masumoto.pdf](https://www.jamstec.go.jp/ceist/j/publication/journal/jes_vol.1/pdf/JES1-3.2-masumoto.pdf)

899 Masumoto, Y. (2010). Sharing the results of a high-resolution ocean general circulation model under  
900 a multi-discipline framework—a review of OFES activities. *Ocean Dynamics*, 60(3), 633–652.  
901 <https://doi.org/10.1007/s10236-010-0297-z>

902 Maurer, T. L., Plant, J. N., & Johnson, K. S. (2021). Delayed-Mode Quality Control of Oxygen, Nitrate,  
903 and pH Data on SOCCOM Biogeochemical Profiling Floats. *Frontiers in Marine Science*, 8.  
904 <https://doi.org/10.3389/fmars.2021.683207>

905 Nakamura, T., & Awaji, T. (2004). Tidally induced diapycnal mixing in the Kuril Straits and its role  
906 in water transformation and transport: A three-dimensional nonhydrostatic model experiment. *Journal*  
907 *of Geophysical Research: Oceans*, 109(C9). <https://doi.org/10.1029/2003JC001850>

908 Nakamura, T., Awaji, T., Hatayama, T., Akitomo, K., Takizawa, T., Kono, T., et al. (2000a). The  
909 Generation of Large-Amplitude Unsteady Lee Waves by Subinertial K1 Tidal Flow: A Possible  
910 Vertical Mixing Mechanism in the Kuril Straits. Retrieved from  
911 [https://journals.ametsoc.org/view/journals/phoc/30/7/1520-](https://journals.ametsoc.org/view/journals/phoc/30/7/1520-0485_2000_030_1601_tgolau_2.0.co_2.xml)  
912 [0485\\_2000\\_030\\_1601\\_tgolau\\_2.0.co\\_2.xml](https://journals.ametsoc.org/view/journals/phoc/30/7/1520-0485_2000_030_1601_tgolau_2.0.co_2.xml)

913 Nakamura, T., Awaji, T., Hatayama, T., Akitomo, K., & Takizawa, T. (2000b). Tidal Exchange  
914 through the Kuril Straits. Retrieved from [https://journals.ametsoc.org/view/journals/phoc/30/7/1520-](https://journals.ametsoc.org/view/journals/phoc/30/7/1520-0485_2000_030_1622_tetts_2.0.co_2.xml)  
915 [0485\\_2000\\_030\\_1622\\_tetts\\_2.0.co\\_2.xml](https://journals.ametsoc.org/view/journals/phoc/30/7/1520-0485_2000_030_1622_tetts_2.0.co_2.xml)

916 Nicholson, D. P., & Feen, M. L. (2017). Air calibration of an oxygen optode on an underwater glider.  
917 *Limnology and Oceanography: Methods*, 15(5), 495–502. <https://doi.org/10.1002/lom3.10177>

918 Ogata, T., & Nonaka, M. (2020). Mechanisms of Long-Term Variability and Recent Trend of Salinity  
919 Along 137°E. *Journal of Geophysical Research: Oceans*, 125(2), e2019JC015290.  
920 <https://doi.org/10.1029/2019JC015290>

921 Pacanowski, R. C., and S. M. Griffies (2000), MOM 3.0 Manual, Technical Report 4, 680 pp., Geophys.  
922 Fluid Dyn. Lab., Princeton, N. J. Philander, S. G. H. (1990), El Niño, La Niña, and the Southern  
923 Oscillation, pp. 293, Academic Press, San Diego, Calif.

924 Pörtner, H. O., & Farrell, A. P. (2008). Physiology and Climate Change. *Science*, 322(5902), 690–692.  
925 <https://doi.org/10.1126/science.1163156>

926 Pozo Buil, M., & Di Lorenzo, E. (2017). Decadal dynamics and predictability of oxygen and  
927 subsurface tracers in the California Current System. *Geophysical Research Letters*, 44(9), 4204–4213.  
928 <https://doi.org/10.1002/2017GL072931>

929 Reid, J. L. (1997). On the total geostrophic circulation of the pacific ocean: flow patterns, tracers, and  
930 transports. *Progress in Oceanography*, 39(4), 263–352. [https://doi.org/10.1016/S0079-](https://doi.org/10.1016/S0079-6611(97)00012-8)  
931 [6611\(97\)00012-8](https://doi.org/10.1016/S0079-6611(97)00012-8)

932 Roemmich, D., & Gilson, J. (2009). The 2004–2008 mean and annual cycle of temperature, salinity,  
933 and steric height in the global ocean from the Argo Program. *Progress in Oceanography*, 82(2), 81–  
934 100. <https://doi.org/10.1016/j.pocean.2009.03.004>

935 Sampaio, E., Santos, C., Rosa, I. C., Ferreira, V., Pörtner, H.-O., Duarte, C. M., et al. (2021). Impacts  
936 of hypoxic events surpass those of future ocean warming and acidification. *Nature Ecology &*  
937 *Evolution*, 5(3), 311–321. <https://doi.org/10.1038/s41559-020-01370-3>

938 Sasaki, H., Nonaka, M., Masumoto, Y., Sasai, Y., Uehara, H., & Sakuma, H. (2008). An Eddy-  
939 Resolving Hindcast Simulation of the Quasiglobal Ocean from 1950 to 2003 on the Earth Simulator.  
940 In K. Hamilton & W. Ohfuchi (Eds.), *High Resolution Numerical Modelling of the Atmosphere and*  
941 *Ocean* (pp. 157–185). New York, NY: Springer. [https://doi.org/10.1007/978-0-387-49791-4\\_10](https://doi.org/10.1007/978-0-387-49791-4_10)

942 Sasano, D., Takatani, Y., Kosugi, N., Nakano, T., Midorikawa, T., & Ishii, M. (2015). Multidecadal  
943 trends of oxygen and their controlling factors in the western North Pacific. *Global Biogeochemical*  
944 *Cycles*, 29(7), 935–956. <https://doi.org/10.1002/2014GB005065>

945 Sasano, D., Takatani, Y., Kosugi, N., Nakano, T., Midorikawa, T., & Ishii, M. (2018). Decline and  
946 Bidecadal Oscillations of Dissolved Oxygen in the Oyashio Region and Their Propagation to the  
947 Western North Pacific. *Global Biogeochemical Cycles*, 32(6), 909–931.  
948 <https://doi.org/10.1029/2017GB005876>

949 Schmidtko, S., Stramma, L., & Visbeck, M. (2017). Decline in global oceanic oxygen content during  
950 the past five decades. *Nature*, 542(7641), 335–339. <https://doi.org/10.1038/nature21399>

951 Sharp, J. D., Fassbender, A. J., Carter, B. R., Johnson, G. C., Schultz, C., Dunne, J. P. (2022). GOBAI-  
952 O<sub>2</sub>: A Global Gridded Monthly Dataset of Ocean Interior Dissolved Oxygen Concentrations Based on  
953 Shipboard and Autonomous Observations (NCEI Accession 0259304). NOAA National Centers for  
954 Environmental Information. Dataset. <https://doi.org/10.25921/z72m-yz67>.

955 Sharp, J. D., Fassbender, A. J., Carter, B. R., Johnson, G. C., Schultz, C., & Dunne, J. P. (2023).  
956 GOBAI-O<sub>2</sub>: temporally and spatially resolved fields of ocean interior dissolved oxygen over nearly 2  
957 decades. *Earth System Science Data*, 15(10), 4481–4518. <https://doi.org/10.5194/essd-15-4481-2023>

958 Stramma, L., Johnson, G. C., Sprintall, J., & Mohrholz, V. (2008). Expanding Oxygen-Minimum  
959 Zones in the Tropical Oceans. *Science*, 320(5876), 655–658. <https://doi.org/10.1126/science.1153847>

960 Stramma, L., Schmidtko, S., Bograd, S. J., Ono, T., Ross, T., Sasano, D., & Whitney, F. A. (2020).  
961 Trends and decadal oscillations of oxygen and nutrients at 50 to 300&thinsp;m depth in the equatorial  
962 and North Pacific. *Biogeosciences*, 17(3), 813–831. <https://doi.org/10.5194/bg-17-813-2020>

963 Stramma, L., & Schmidtko, S. (2021). Tropical deoxygenation sites revisited to investigate oxygen  
964 and nutrient trends. *Ocean Science*, 17(3), 833–847. <https://doi.org/10.5194/os-17-833-2021>

965 Suga, T., Takei, Y., & Hanawa, K. (1997). Thermostad Distribution in the North Pacific Subtropical  
966 Gyre: The Central Mode Water and the Subtropical Mode Water. Retrieved from  
967 [https://journals.ametsoc.org/view/journals/phoc/27/1/1520-](https://journals.ametsoc.org/view/journals/phoc/27/1/1520-0485_1997_027_0140_tditnp_2.0.co_2.xml)  
968 [0485\\_1997\\_027\\_0140\\_tditnp\\_2.0.co\\_2.xml](https://journals.ametsoc.org/view/journals/phoc/27/1/1520-0485_1997_027_0140_tditnp_2.0.co_2.xml)

969 Suga, T., Motoki, K., Aoki, Y., & Macdonald, A. M. (2004). The North Pacific Climatology of Winter  
970 Mixed Layer and Mode Waters. Retrieved from  
971 [https://journals.ametsoc.org/view/journals/phoc/34/1/1520-  
972 0485\\_2004\\_034\\_0003\\_tnpcow\\_2.0.co\\_2.xml](https://journals.ametsoc.org/view/journals/phoc/34/1/1520-0485_2004_034_0003_tnpcow_2.0.co_2.xml)

973 Takatani, Y., Sasano, D., Nakano, T., Midorikawa, T., & Ishii, M. (2012). Decrease of dissolved  
974 oxygen after the mid-1980s in the western North Pacific subtropical gyre along the 137°E repeat  
975 section. *Global Biogeochemical Cycles*, 26(2). <https://doi.org/10.1029/2011GB004227>

976 Takeshita, Y., Martz, T. R., Johnson, K. S., Plant, J. N., Gilbert, D., Riser, S. C., et al. (2013). A  
977 climatology-based quality control procedure for profiling float oxygen data. *Journal of Geophysical  
978 Research: Oceans*, 118(10), 5640–5650. <https://doi.org/10.1002/jgrc.20399>

979 Udaya Bhaskar, T. V. S., Sarma, V. V. S. S., & Pavan Kumar, J. (2021). Potential Mechanisms  
980 Responsible for Spatial Variability in Intensity and Thickness of Oxygen Minimum Zone in the Bay  
981 of Bengal. *Journal of Geophysical Research: Biogeosciences*, 126(6), e2021JG006341.  
982 <https://doi.org/10.1029/2021JG006341>

983 Winkler, L. W. (1888). Die Bestimmung des im Wasser gelösten Sauerstoffes. *Berichte Der Deutschen  
984 Chemischen Gesellschaft*, 21(2), 2843–2854. <https://doi.org/10.1002/cber.188802102122>

985 Wolf, M. K., Hamme, R. C., Gilbert, D., Yashayaev, I., & Thierry, V. (2018). Oxygen Saturation  
986 Surrounding Deep Water Formation Events in the Labrador Sea From Argo-O<sub>2</sub> Data. *Global  
987 Biogeochemical Cycles*, 32(4), 635–653. <https://doi.org/10.1002/2017GB005829>

988 Xu, L., Wang, K., & Wu, B. (2022). Weakening and Poleward Shifting of the North Pacific Subtropical  
989 Fronts from 1980 to 2018. *Journal of Physical Oceanography*, 52(3), 399-417.  
990 <https://doi.org/https://doi.org/10.1175/JPO-D-21-0170.1>

991 Yang, H., Lohmann, G., Krebs-Kanzow, U., Ionita, M., Shi, X., Sidorenko, D., et al. (2020). Poleward  
992 Shift of the Major Ocean Gyres Detected in a Warming Climate. *Geophysical Research Letters*, 47(5),  
993 e2019GL085868. <https://doi.org/10.1029/2019GL085868>

994 Yasuda, I. (2004). North Pacific Intermediate Water: Progress in SAGE (SubArctic Gyre Experiment)  
995 and Related Projects. *Journal of Oceanography*, 60(2), 385–395.  
996 <https://doi.org/10.1023/B:JOCE.0000038344.25081.42>

997 You, Y. (2003). The pathway and circulation of North Pacific Intermediate Water. *Geophysical*  
998 *Research Letters*, 30(24). <https://doi.org/10.1029/2003GL018561>

999

1000

1001